Original Paper

Implications for fault reactivation and seismicity induced by hydraulic fracturing

Zi-Han Sun [a], Ming-Guang Che [b, *], Li-Hong Zhu [c], Shu-Juan Zhang [c, **], Ji-Yuan Lu [c], Chang-Yu Jin [a]

[a] *Key Laboratory of Ministry of Education on Safe Mining of Deep Metal Mines, School of Resources and Civil Engineering and Key Laboratory of Liaoning Province on Deep Engineering and Intelligent Technology, Northeastern University, Shenyang, 110819, Liaoning, China*
[b] *Research Institute of Petroleum Exploration & Development, PetroChina Company Limited, Beijing, 100084, China*
[c] *The Exploration and Development Research Institute of Daqing Oilfield Limited Company, Daqing, 163458, Heilongjiang, China*

ARTICLE INFO

ABSTRACT

Evaluating the physical mechanisms that link hydraulic fracturing (HF) operations to induced earthquakes and the anticipated form of the resulting events is significant in informing subsurface fluid injection operations. Current understanding supports the overriding role of the effective stress magnitude in triggering earthquakes, while the impact of change rate of effective stress has not been systematically addressed. In this work, a modified critical stiffness was brought up to investigate the likelihood, impact, and mitigation of induced seismicity during and after hydraulic fracturing by developing a poroelastic model based on rate-and-state fraction law and linear stability analysis. In the new criterion, the change rate of effective stress was considered a key variable to explore the evolution of this criterion and hence the likelihood of instability slip of fault. A coupled fluid flow—deformation model was used to represent the entire hydraulic fracturing process in COMSOL Multiphysics. The possibility of triggering an earthquake throughout the entire hydraulic fracturing process, from fracturing to cessation, was investigated considering different fault locations, orientations, and positions along the fault. The competition between the effects of the magnitude and change rate of effective stress was notable at each fracturing stage. The effective stress magnitude is a significant controlling factor during fracturing events, with the change rate dominating when fracturing is suddenly started or stopped. Instability dominates when the magnitude of the effective stress increases (constant injection at each fracturing stage) and the change rate of effective stress decreases (the injection process is suddenly stopped). Fracturing with a high injection rate, a fault adjacent to the hydraulic fracturing location and the position of the junction between the reservoir and fault are important to reduce the Coulomb failure stress (CFS) and enhance the critical stiffness as the significant disturbance of stresses at these positions in the coupled process. Therefore, notable attention should be given to the injection rate during fracturing, fault position, and position along faults as important considerations to help reduce the potential for induced seismicity. Our model was verified and confirmed using the case of the Longmaxi Formation in the Sichuan Basin, China, in which the reported microseismic data were correlated with high critical stiffness values. This work supplies new thoughts of the seismic risk associated with HF engineering.

© 2024 The Authors. Publishing services by Elsevier B.V. on behalf of KeAi Communications Co. Ltd. This is an open access article under the CC BY-NC-ND license (http://creativecommons.org/licenses/by-nc-nd/4.0/).

1. Introduction

Shale gas, as an important product of unconventional reservoirs (Xu et al., 2015; Jiang et al., 2017; Celleri and Sánchez, 2021; Rezlerova et al., 2021), was considered inaccessible in low-permeability formations (Peduzzi and Harding, 2013; Yehya et al., 2018, 2022). The extraction of shale gas has become economically

feasible in recent years through the advent of horizontal drilling and massive hydraulic fracturing (HF) operations. The HF process is achieved by drilling a horizontal well followed by pressurizing the cased well with a mixture of fluids and proppant, namely, HF fluid (Davis and Fisk, 2017). The HF technique is recognized as the predominant method of subsurface engineering operations gas drainage, and geothermal resource development because it enhances the permeability of reservoirs and effectively stimulates the flow of hydrocarbons into wells (Peduzzi and Harding, 2013; Meng et al., 2021).

However, as subsurface engineering proliferates and increases in scale, the number of induced seismic events related to different anthropogenic activities increases in addition to the vast majority of natural earthquakes occurring each year (Frohlich, 2012; van Thienen-Visser et al., 2018; Benson et al., 2020; Yehya et al., 2022). According to statistics of the Human-induced earthquakes (HiQuake), by March 2023, a total of 1294 human-induced earthquakes with a magnitude M_w of $-2.2-7.9$ occurred worldwide (HiQuake, 2023). It is publicly available at www.inducedearthquakes.org. Among them, 33% of induced earthquakes were clearly associated with fracturing operations, such as in the Sichuan Basin, China, and central and eastern United States (Bao and Eaton, 2016; Sheng et al., 2022; Li et al., 2023). Therefore, induced earthquake events during HF operations have resulted in increasing public concern regarding environmental and safety issues worldwide (Bao and Eaton, 2016; Lei et al., 2017; Brudzinski and Kozowska, 2019; Atkinson et al., 2020; Sheng et al., 2020; Wang et al., 2020; Chen et al., 2021).

HF is a complex subsurface coupled fluid flow–deformation process and involves not only the improvement in the reservoir permeability but also the variation in stress and strain within the existing fault system in the formation under the effect of the fluid pressure (Ellsworth, 2013; Wang et al., 2016; Benson et al., 2020; Villa and Singh, 2020). In other words, the injection of fluids into a low-permeability formation (i.e., HF operation) not only has the potential to enhance the reservoir permeability but also has the potential to alter the fault stress state under normal stress deflection, reactivate faults, and induce seismicity (Ellsworth, 2013). A growing number of field observations suggest that HF operations are corelated in space and time with nearby detected seismicity (Davies et al., 2013; Holland, 2013; Bao and Eaton, 2016; Deng et al., 2016; Schultz et al., 2017; Brudzinski and Kozowska, 2019), such as in the Longmaxi Formation, Sichuan Basin, China. In experimental (Eyre et al., 2019; Shan et al., 2021) and theoretical studies (Gan and Lei, 2020; Chen et al., 2021), the link between HF operations and triggering seismicity has been investigated. However, we still lack a thorough understanding of the potential for triggering seismic events during and after HF operations, including the mechanisms of HF-induced earthquakes on the one hand and the impacts of *in situ* conditions and fracture properties on the likelihood of triggering seismic events on the other hand.

The occurrence region of these injection-induced earthquakes can usually not be obtained based on the HF operation period and area (Bachmann et al., 2011; Mignan et al., 2015; Kim et al., 2018; Sun et al., 2017). However, the stratigraphic characteristics and distribution of faults in formations play a main role in determining the likelihood of inducing earthquakes (Yehya et al., 2022). In previous works, two major physical mechanisms of triggered an earthquake during fluid injection have been considered. One mechanism suggests that the pore fluid pressure diffuses through the rock matrix until it reaches a critically stressed fault core within the damage zone (Ellsworth, 2013; Schultz et al., 2014; Galloway et al., 2018; Hui et al., 2021). Based on the Mohr–Coulomb criterion, the enhancement in pore pressure in the fault core reduces the effective stress and shear friction strength, thus facilitating

unstable fault slip that could induce earthquakes (Terzaghi, 1923; Ji et al., 2022). The other mechanism involves the changes in stress in the existing fault core due to the solid matrix response to fluid injection according to the effective stress law (Terzaghi, 1923), thus triggering unstable fault slip and inducing earthquakes (Chang and Segall, 2016a, 2016b; Keranen et al., 2014; Segall and Lu, 2015; Barbour et al., 2017). The premise of these two mechanisms is that a critically stressed fault must occur in the formation and that fault reactivation occurs due to the change in the stress state during fluid injection for injection-induced seismic events to arise (Alghannam and Juanes, 2020; Yehya et al., 2022).

The change in the Coulomb failure stress (CFS) is commonly used as a failure criterion for analysing fault reactivation by fluid injection (Vilarrasa et al., 2016; Yehya et al., 2018; Fan et al., 2019). Based on the CFS failure criterion, any natural or anthropogenic activity that alters the shear stress, normal stress or pore pressure can drive critically stressed faults towards failure (Fig. 1) (Brudy et al., 1997; Zoback and Harjes, 1997; Townend and Zoback, 2000). The variation in the CFS value disturbs dormant faults and promotes fault reactivation (Zoback and Harjes, 1997; Evans et al., 2012; Yehya et al., 2022). This criterion can only predict whether a given fault can be reactivated but cannot determine whether fault slip will result in an aseismic response via creep-sliding or a seismic response via stick-sliding, i.e., whether fault slip will trigger earthquakes (Warpinski et al., 2012; Goodfellow et al., 2015; Guglielmi et al., 2015; Fan et al., 2019). Thus, the likelihood of injection-induced earthquakes cannot be comprehensively evaluated only by CFS as it can only determine the reactivate behaviour of fault (Yehya et al., 2022).

In view of this defect, the use of a model combined with rate-and-state friction (RSF) theory and the single-degree-of-freedom spring-slider model overcomes this disadvantage (Ruina and Andy, 1983; Tullis and Weeks, 1986; Linker and Dieterich, 1992; Rice, 1993; Ruina, 1983; Alghannam and Juanes, 2020; Lu et al., 2023). RSF theory can be used to characterize the stability of frictional sliding and the evolution of slip behaviour by evaluating the dependence of the friction velocity (Dieterich, 1972; Dieterich, 1978; Hutka et al., 2023). The frictional strength decreases with increasing shear slip, and the fault exhibits the potential for earthquake nucleation. Conversely, the likelihood of an aseismic response of the fault increases, the concept of the critical stiffness of the fault, obtained from the combination of RSF theory and simple spring-slider models (Ruina, 1983; Tullis and Weeks, 1986; Rice, 1993; Lu et al., 2023), is extensively applied to determine the likelihood of injection-induced earthquakes. In the classical model, it is composed of several parameters, obtained from direct/double experiment, controlling the transition from stable to unstable sliding (Gu et al., 1984; Rice, 1993; Leeman et al., 2016; van den Ende et al., 2018; Alghannam and Juanes, 2020). Recently, a modified critical stiffness constitutive law was proposed by Alghannam and Juanes (2020) to account for the effect of variations in the pressurization rate on the likelihood of inducing seismicity. However, the effect of the transient change in the normal stress resulting from fluid injection on the likelihood of triggering earthquakes has remained highly overlooked (Improta et al., 2015; Tang et al., 2018).

Observations for the field monitoring data have further shown that unstable fault slip during injection-induced earthquakes can occur either by pore pressure diffusion along the damage zone or poroelasticity deformation through the rock matrix near reactivated existing faults (Rice and Cleary, 1976; Fisher and Warpinski, 2012; Deng et al., 2016; Tang et al., 2018; Ji et al., 2022). However, during HF operations, only changes in the pore pressure are unlikely to cause induced seismic events, as the pore pressure requires time to diffuse and reach faults during injection transformation and
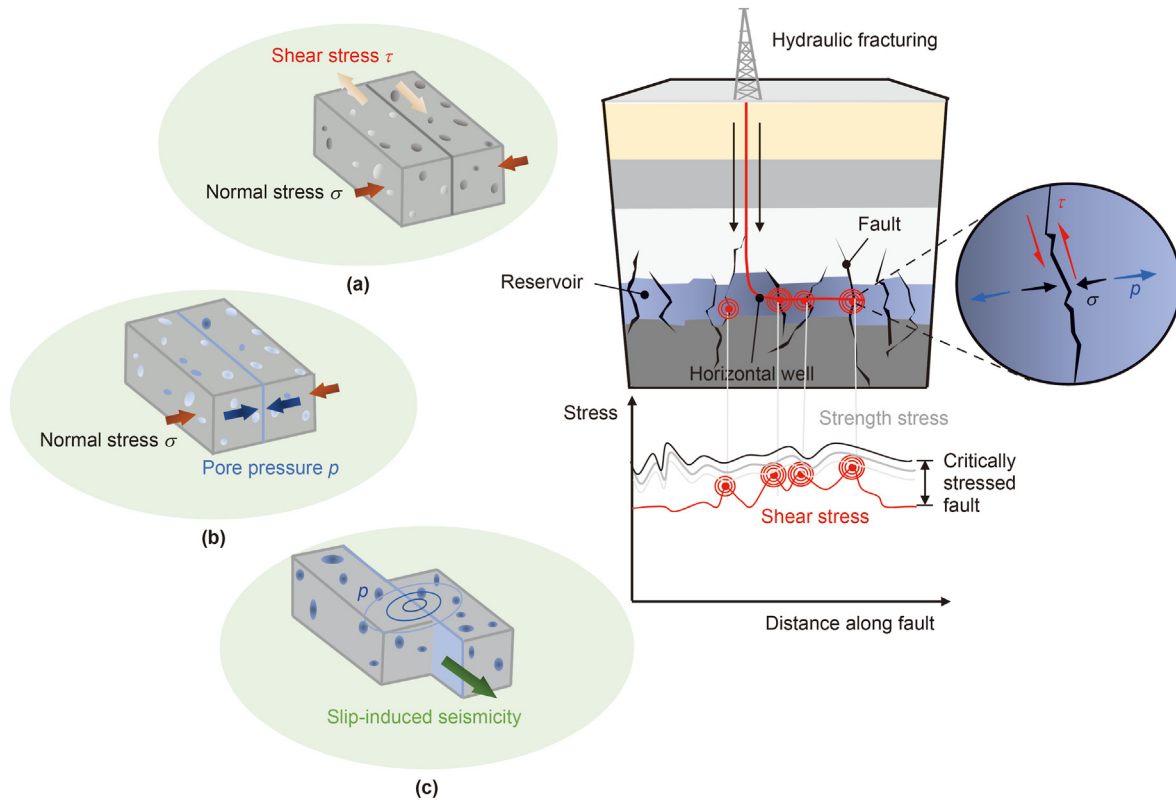
Fig. 1. Schematic of the fault reactivation mechanism during hydraulic fracturing, where τ is the shear stress, σ is the normal stress, and p is the pore pressure. Post fluid injection, three stages can be observed in the variation of stress applied on the fault: (i) In Stage (a), the fluid is injected and then diffuses into the reservoir but does not arrive to the fault. The frictional shear strength of the fault is determined by the normal stress on fault. (ii) In Stage (b), the fluid diffuses and arrives to the fault. The pore pressure of fault increases and the frictional shear strength of fault decreases. The fault is more prone to slipping. (iii) In Stage (c), the frictional shear strength cannot resist the shear stress of fault. The fault slips.

stopping (Bao and Eaton, 2016; Deng et al., 2016; Galloway et al., 2018; Yehya et al., 2022). The shear stress and normal stress of the rock matrix near the fault vary instantly and significantly and induce stress deflection in critically stressed faults, thus triggering earthquakes (Gudmundsson, 2022).

The above observations further demonstrate that most studies focused on the effect of the fault normal stress magnitude on the likelihood of induced earthquakes in the fracturing process (Gu et al., 1984; Rice, 1993; Leeman et al., 2016). For example, Yehya et al. (2018) assessed the seismic response of faults to HF operations by estimating the change in the CFS value along a fault in the Duvernay Formation, Alberta, Western Canada. However, the change rate of the fault normal stress resulting from the variable fluid injection rate during HF operation has remained overlooked in revealing the mechanism of injection-induced earthquakes (Rice, 1993; Alghannam and Juanes, 2020). Furthermore, the coupled effects on deformation and diffusion in reservoirs and faults during fracturing must be considered to appropriately reproduce the full coupling between solid poroelastic deformation and fluid flow. The spatiotemporal characteristics of the observed microseismicity signals indicated that the seismic events along the fault at the first three fracturing stages were directly related to the injection process, while the detected seismic events were attributed to fault relaxation after the fourth fracturing stage (Zhang et al., 2020).

In this study, to accurately predict the likelihood of HF-induced earthquakes, we developed a modified fault critical stiffness criterion that considers the effect of the magnitude and change rate of effective stress. We focused on the effects of the fault location, orientation, and different positions along the fault on the critical stiffness and the relationship among the CFS value, fault critical stiffness and earthquake triggering. We estimated the fully coupled process during HF operations using a three-dimensional finite element poroelastoplastic model in COMSOL Multiphysics. Furthermore, we considered a case study of the Longmaxi Formation shale in Changning, Yibin, Sichuan, southwestern China, where seismic events were reported during and after HF operations, to relate the fault response to real seismic data. We analysed and verified that the variations in the CFS value and critical stiffness of the fault are correlated with the microseismic activities observed at various fracturing stages. The new approach and results are reported below.

2. Mathematical model

In the model, the reservoir, fault, and wall rock matrix are approximated as poroelastic media (Biot, 1941) to investigate the poroelastic coupling of stresses of the fault and characterize the effect of changes in stress on triggering earthquakes during HF operations using the fault critical stiffness (Alghannam and Juanes, 2020; Yehya et al., 2022).

2.1. Coupled poroelastic model

2.1.1. Governing equation of deformation

The relationship of the deformation for the reservoir and fault can be defined as (Detournay, 1993; Cui et al., 2018)

$$G_m u_{i,kk} + \frac{G_m}{1-2\nu} u_{k,ki} = f_i + \alpha_m p_m \tag{1}$$

where G_m represents the shear modulus; u and α_m are the displacement and Biot coefficient, respectively; p_m is the gas pressure; subscript m denotes the form of the medium as either a fault or a reservoir; subscripts i and k denote the directional components of the variables; subscript kk denotes the Einstein summation convention; subscripted comma denotes the time derivative of a variable; subscript ki denotes the interchanging indices, representing the components of strain with different directions. The right side of Eq. (1) represents the body force per unit volume resulting from fluid injection.

2.1.2. Governing equation of fluid flow

In this work, the single-phase flow is assumed and mass conservation law together with Darcy's law and storage model is written as (Biot, 1941; Darcy, 1856)

$$\rho_m S \frac{\partial(p_m)}{\partial t} + \rho_m \alpha \frac{\partial(\varepsilon_v)}{\partial t} = \nabla \cdot \left(\rho_m \frac{k_m}{\mu_v} (\nabla p_m - \rho_m g) \right) \tag{2}$$

$$S = \phi_m \chi_f + (1 - \phi_m)\chi_p \tag{3}$$

where ρ_m represents the fluid density; S is the storage coefficient; ϕ_m denotes the porosity of matrix; χ_f is the compressibility of the fluid; χ_p is the effective compressibility of the matrix; α is the Biot coefficient; ε_v is the volumetric strain; k_m is the permeability of both the reservoir and fault; μ_v is the dynamic viscosity; g is the gravitational acceleration.

2.2. Coulomb failure stress criterion

The normal stress component σ and the shear stress component τ acting on the fault can be defined in the form of Cauchy's stress. The stress vector $\overset{n}{\boldsymbol{T}}$ can be expressed as the components of the stress tensor σ_{ij} at a given point (Teodor and Ardéshir, 2000). The magnitude of the normal stress component σ can be obtained as

$$\sigma = \overset{n}{\boldsymbol{T}} \cdot n = \overset{n}{T_i} \cdot n_i \tag{4}$$

with

$$\overset{n}{T_i} = \sigma_{ij} n_j$$

Eq. (4) can be expressed as follows:

$$\sigma = \sigma_{ij} n_i n_j \quad \text{or} \quad \sigma = \overset{n}{T_x} n_x + \overset{n}{T_y} n_y + \overset{n}{T_z} n_z \tag{5}$$

The magnitude of the shear stress component τ can be determined as

$$\tau = (\overset{n}{T})^2 - \sigma^2 \tag{6}$$

Based on the definition of $\overset{n}{T}()$, $(\overset{n}{T})^2$ can be obtained as

$$(\overset{n}{T})^2 = \overset{n}{\boldsymbol{T}} \times \overset{n}{\boldsymbol{T}} = \overset{n}{T_i}\overset{n}{T_i} = (\sigma_{ij}n_j)(\sigma_{ik}n_k) \quad \text{or} \quad (\overset{n}{T})^2 = \sigma_{ij}\sigma_{ik}n_j n_k \tag{7}$$

Eqs. (5) and (6) denote the normal stress σ and shear stress τ, respectively, on an arbitrary plane.

We use the CFS parameter to assess the potential of fault reactivation, and any positive change in the CFS value impacts the response of the fault to HF injection perturbation, which could lead to fault slip. For a cohesionless fault, the change in CFS can be defined as

$$\Delta CFS = \Delta\tau - \mu_f(\Delta\sigma - \Delta p) \tag{8}$$

where μ_f is the coefficient of static friction; $\Delta\tau$ denotes the change in the shear stress; $\Delta\sigma - \Delta p$ denotes the change in the effective stress; $\Delta\sigma$ and Δp denote the changes in the normal stress and the pore pressure acting on the fault, respectively, based on the Mohr–Coulomb model combined with the effective stress law (Terzaghi, 1923). We assumed that compression is positive and tension is negative. Any natural or anthropogenic activity that alters the shear stress, normal stress or pore pressure could cause critically stressed faults to fail (Townend and Zoback, 2000; Bao and Eaton, 2016; Villa and Singh, 2020). We note that this Coulomb stress change criterion addresses fault stability without distinguishing whether the resulting fault slip is seismic or aseismic.

2.3. Modified critical stiffness

The classical critical stiffness of fault in the original study (Rice, 1993) (which is defined as $K_{crit} = (\sigma - p)(b - a)/d_c$, where $b - a$ is the friction stability parameter and d_c is the critical slip distance for state evolution) was considered to be determined by the magnitude of effective stress. The likelihood of injection-induced earthquakes rises with the increase in effective stress. In recent years, engineering field data reports that abrupt changes in injection rate and the occurrence of earthquakes are highly correlated (Kim, 2013; Tang et al., 2018). The critical stiffness regarding the effect of change rate of pore pressure (which is defined as $K_{crit} = (\sigma - p)(b - a)/d_c + \alpha\dot{p}/v_0$, where $\dot{p}$ is the change rate of the pore pressure and v_0 and α are the initial velocity and an empirical scaling factor, respectively) was thus proposed by Alghannam and Juanes (2020) to explain these observations.

However, the effect of the change in the normal stress on the likelihood of triggering earthquakes has been ignored in existing research. In this section, we modified the critical stiffness criterion by including the change rate of effective stress based on the RSF theory and spring-slider model.

2.3.1. Rate- and state-dependent friction

A spring-slider model can express the variation of effective stress in the whole process of fault slip (Rice, 1993; Cueto-Felgueroso et al., 2017; Alghannam and Juanes, 2020; Lu et al., 2023). As shown in Fig. 2, the spring-slider model composes a slider forced by a spring, which represents the combined geometric fault stiffness.

The shear strength of the fault, τ_f, can be obtained by the Mohr–Coulomb model (Pampillon et al., 2018):

$$\tau_f = \mu(v, \theta)(\sigma - p) + \tau_c \tag{9}$$

where $\mu(v, \theta)$ represents the friction coefficient and is defined based on Ruina's slip law (Ruina and Andy, 1983); τ_c is the cohesive strength (hereafter, $\tau_c = 0$); $\sigma - p$ denotes the effective contact pressure; σ and p are the normal stress and pore pressure, respectively, that act on the fault and reservoir. Here, we assumed that compression is positive.

The tractive force of the slider is defined as the difference between the shear stress and the shear friction strength of fault (Segall and Rice, 1995; Iverson, 2005; Mitsui and Cocco, 2010; Chen and Niemeijer, 2017; Alghannam and Juanes, 2020). The momentum balance equations for the effective stress variation in the spring-slider model can be defined as (Rice and Ruina, 1983; Segall and Rice, 1995; Alghannam and Juanes, 2020; Sun et al., 2023)
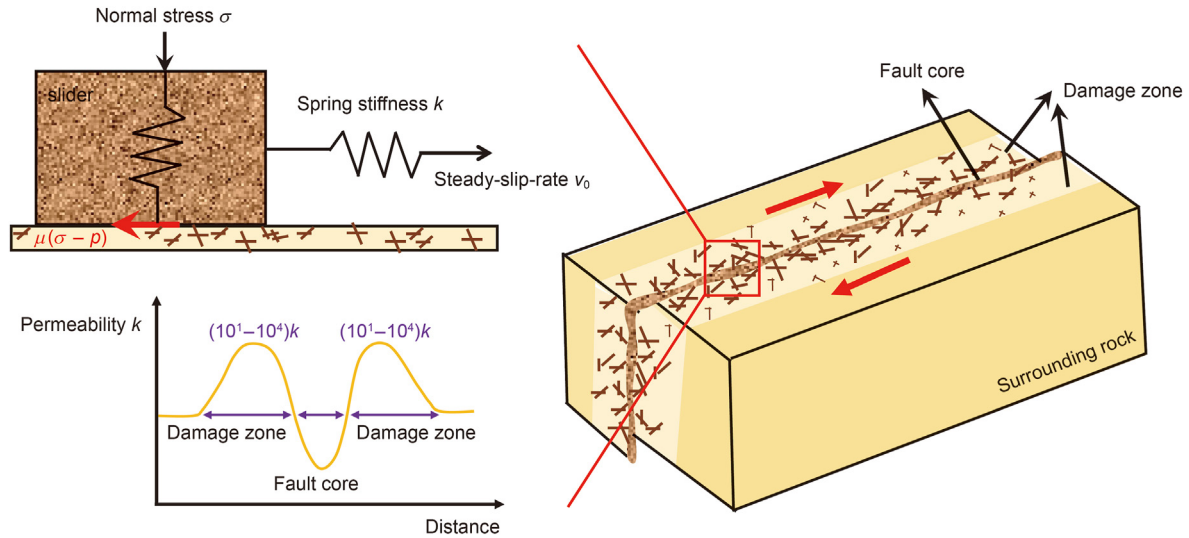
Fig. 2. Conceptual model of a strike-slip fault connected with a spring-slider model and the typical permeability distribution within the fault damage zone and core.

$$\tau_{\mathrm{f}} - \kappa_{\mathrm{s}}U = 0 \tag{10}$$

$$\dot{U} = v_0 - v \tag{11}$$

where U is the displacement from v_0 to v; and κ_{s} is the shear stiffness of the spring-slider system.

Ruina's slip law is achieved by the coefficient of friction (Ruina and Andy, 1983):

$$\mu(v, \theta) = \mu^* + a\ln\frac{v}{v^*} + \theta \tag{12}$$

where a is the friction constitutive parameter; v^* is the normalized velocity; μ^* is a constant that is appropriate for the steady state at velocity v^*; and θ is the state variable.

Rate-and-rate model proposed by Linker and Dieterich (1992) integrates the effective stress principle, which can be expressed as follows:

$$\dot{\theta} = -\frac{v}{d_{\mathrm{c}}}(\theta + b\ln\frac{v}{v^*}) - \alpha\frac{\dot{\sigma} - \dot{p}}{\sigma - p} \tag{13}$$

where d_{c} is the characteristic distance; b is a constitutive parameter (indirect effect); α is an empirical scaling factor; $\sigma - p$ is the effective stress magnitude; and $\dot{\sigma} - \dot{p}$ is the change rate of effective stress.

2.3.2. Linear stability analysis

To quantify the variation in the effective stress, a linear stability analysis of the system was conducted in the quasi-steady state in which sliding remained constant, but the effective stress evolved. Eqs. (12) and (13) were linearized to a quasi-steady state and substituted into Eq. (10), resulting in the following:

$$\sigma\theta^* + \frac{\alpha v^*(\sigma - p)}{v_0} = \kappa_{\mathrm{s}}U^* \tag{14}$$

where θ^* is the normalized state variable.

Adding the time derivative of Eq. (12) yields the following:

$$\dot{v}^* = \frac{v_0}{a(\sigma - p)}\left[-\frac{\alpha(\dot{\sigma} - \dot{p})}{v_0} + \frac{b(\sigma - p)}{d_{\mathrm{c}}} - \kappa_{\mathrm{s}}\right]v^*$$
$$+ \frac{v_0}{a(\sigma - p)}\left[\frac{v_0(\sigma - p)}{d_{\mathrm{c}}}\right]\theta^* \tag{15}$$

$$\dot{\theta}^* = \left(\frac{\alpha(\dot{\sigma} - \dot{p})}{v_0(\sigma - p)} - \frac{b}{d_{\mathrm{c}}}\right)v^* - \frac{v_0}{d_{\mathrm{c}}}\theta^*$$

The solutions to Eq. (15) are of the forms $\tau^* = ReA_1e^{\lambda t}$ and $\theta^* = ReA_2e^{\lambda t}$, in which Re denotes the real part of the operator, A_1 and A_2 are constants, λ is the growth rate, and t is the time. Substituting the above form into Eq. (15), we can obtain

$$\lambda^2 + \left[\frac{v_0}{d_{\mathrm{c}}} - \frac{v_0}{a(\sigma - p)}\left(-\frac{\alpha(\dot{\sigma} - \dot{p})}{v_0} + \frac{b(\sigma - p)}{d_{\mathrm{c}}} - \kappa_{\mathrm{s}}\right)\right]\lambda$$
$$- \frac{v_0}{a(\sigma - p)}\left[\frac{k_{\mathrm{s}}v_0}{d_{\mathrm{c}}}\right] = 0 \tag{16}$$

When the real part of λ_i is negative for all values of i, the perturbations due to fluid injection are damped, and the system remains stable. In the opposite case, the real part of λ_i is positive for some values of i, the destabilizations increase exponentially, and the system is unstable. According to the discriminant of the above equation root, the following can be obtained

$$K_{\mathrm{crit}} = -\frac{\alpha(\dot{\sigma} - \dot{p})}{v_0} + \frac{(b - a)(\sigma - p)}{d_{\mathrm{c}}} \tag{17}$$

As indicated, two forms, effective stress magnitude ($\frac{(b-a)(\sigma-p)}{d_c}$) and the change rate ($\frac{\alpha(\dot{\sigma}-\dot{p})}{v_0}$), compose the critical stiffness. Accordingly, when the shear stiffness of the fault is higher than its critical stiffness (Eq. (17)), the slider becomes unsteady, and seismic slip of the fault can be triggered. Conversely, the slider remains steady or aseismic slip of the fault is induced.

3. Numerical model setup

We applied the model proposed above to investigate the effect of different factors on the variation of the critical stiffness in the HF process. The proposed model was implemented in—and solved

using—COMSOL Multiphysics (version 5.4). The coupling process of reservoir deformation and fluid flow were achieved through Eqs. (1)–(3) . Darcy's law together with storage model and the deformation equation in Navier term were employed to address fluid diffusion and mechanical deformation in the formation, respectively. In COMSOL Multiphysics (version 5.4), all of the coupling equations (Eqs. (1)–(3)) were solved within a single iteration step.

3.1. Engineering background and model geometry

Horizontal well Ning 201-H1 is located at the southern edge of the Sichuan Basin in Changning, Yibin, Sichuan, southwestern China. Changning, Sichuan Basin, is a lowland region adjacent to the Yungui Plateau to the south and southeast and is flanked by the Tibetan Plateau to the west and northwest (Guo et al., 2011; Liang et al., 2014) (Fig. 3). The target formation of the Ning 201-H1 exploration well is the Yibin Longmaxi Formation shale. The Longmaxi Formation shale in Yibin, Sichuan, with a thickness of 288 m, has been the most successful shale gas exploration play in recent years and is expected to be a major unconventional resource play in China (Zou et al., 2010; Zhao et al., 2016, 2018; Jia et al., 2022). The total length of the Ning 201-H1 well is 3790 m, with a vertical depth of approximately 2000 m. The initial fracturing design of the Ning 201-H1 well involved 12 stages and has been adjusted to include 10 fracturing stages due to engineering problems such as severe casing deformation. The injection rate at each fracturing stage is 9 m^3/s with each injection period lasting approximately 3 h (Zhang et al., 2020). A vertical well, Ning 201, with eight downhole geophones was used to monitor the occurrence of microseismicity.

During HF operations, fault reactivation is evidenced by severe casing deformation (Zhang et al., 2020). The monitored microseismic signals further verified that the fault existing in the formation experienced seismic slip-inducing earthquakes. Therefore, it is very important to investigate the mechanisms of the relationship between HF and induced fault seismic slip to appropriately correct for HF operations.

Fig. 4(a) shows the microseismic events attributed to HF stimulation of well N201-H1 (Zhang et al., 2020). The red oval denotes a pre-existing fault that was activated during stimulation due to its direct connection to the hydraulic fractures. We constructed a geological system represented by a prismatic block (4000 m × 1800 m × 888 m) divided into three smaller blocks represented the reservoir (4000 m × 1800 m × 288 m) and the fault architecture, including both the fault core and the fault-damage zone (in total: 10.1 m × 1800 m × 888 m) as well as the

surrounding rock based on on-site monitoring data analysis (Zhang et al., 2020), as shown in Fig. 4(a). The stress regime is a strike-slip faulting regime, with the value of σ_{Hmax} for the y direction is greatest, followed by σ_v for the z direction, and finally by σ_{hmin} for the x direction (Anderson, 1905). The fault is dipping 30° from the y direction. A conceptual model of the fault zone structure was adopted and involves a 10-cm-wide fault core embedded in a 10-m-wide fault-damage zone (Rice and James, 2006). The lower-permeability fault core is composed of gouges (Caine et al., 1996; Vrolijk et al., 2016). The higher-permeability damage zone contains fractures with different scales and subsidiary faults (Min et al., 2009). The permeability of both the reservoir and the fault-damage zone was set to 1.0 × 10^{-15} m^2, with a value of 1.0 × 10^{-18} m^2 specified for the surrounding rock and fault core.

3.2. Model meshing

A geometric mismatch initially occurred because the width of the fault core was at the scale of fractions of a metre, whereas the reservoir was at the scale of kilometres. To resolve this issue, the mesh was densified towards the fault to achieve a smooth transition from the metre scale to the kilometre scale, as shown in Fig. 4(b). After meshing, the model consisted of 82,346 tetrahedrons and 5460 hexahedrons, with an average element quality of 0.636. The horizontal well was represented by a horizontal line including 10 mass sources, 300 m/1200 m from the fault core and located at the centre along the y direction. Calculation location of numerical simulation was joined with the reservoir and fault core with the same y-coordinate as that of the 10 mass sources, as shown in Fig. 4(a). When the fault is activated due to HF operations, there will be an increase in the permeability of the fault core, which was not considered in this simulation model.

3.3. Boundary conditions and parameters

The solid mechanics and Darcy's law modules in COMSOL Multiphysics were adopted to implement the coupled process of reservoir/fault deformation and fluid diffusion. The fixed feature was applied to the base of the simulation model. The other surfaces of the model were free to deform. Hydraulic fluid was injected into the reservoir, and the pressure pulse diffused horizontally towards the fault. The surrounding boundaries were considered as no-flow boundaries. The injection sources during HF operation were activated one after the other, by injecting 9 m^3/s water per mass source for 3 h followed by 6 h of zero injection. The whole HF operation process was continued for 90 h, followed by a 180-hour shut-off
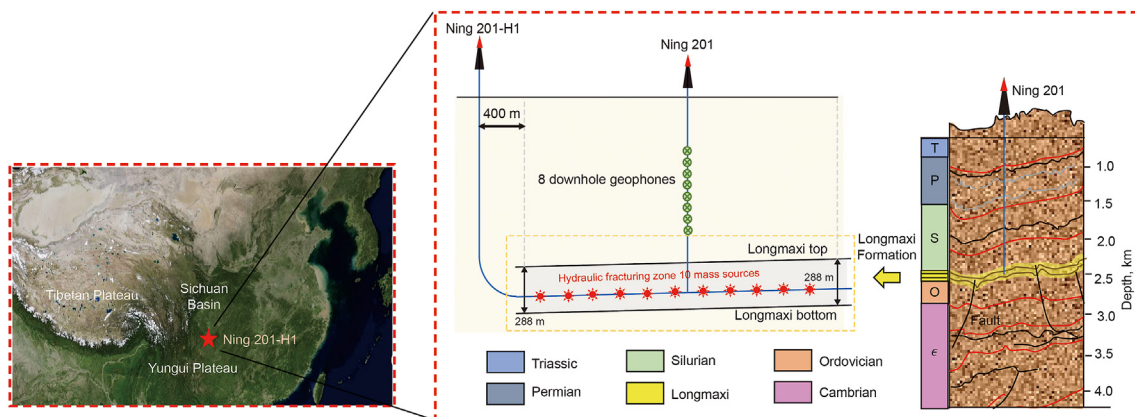

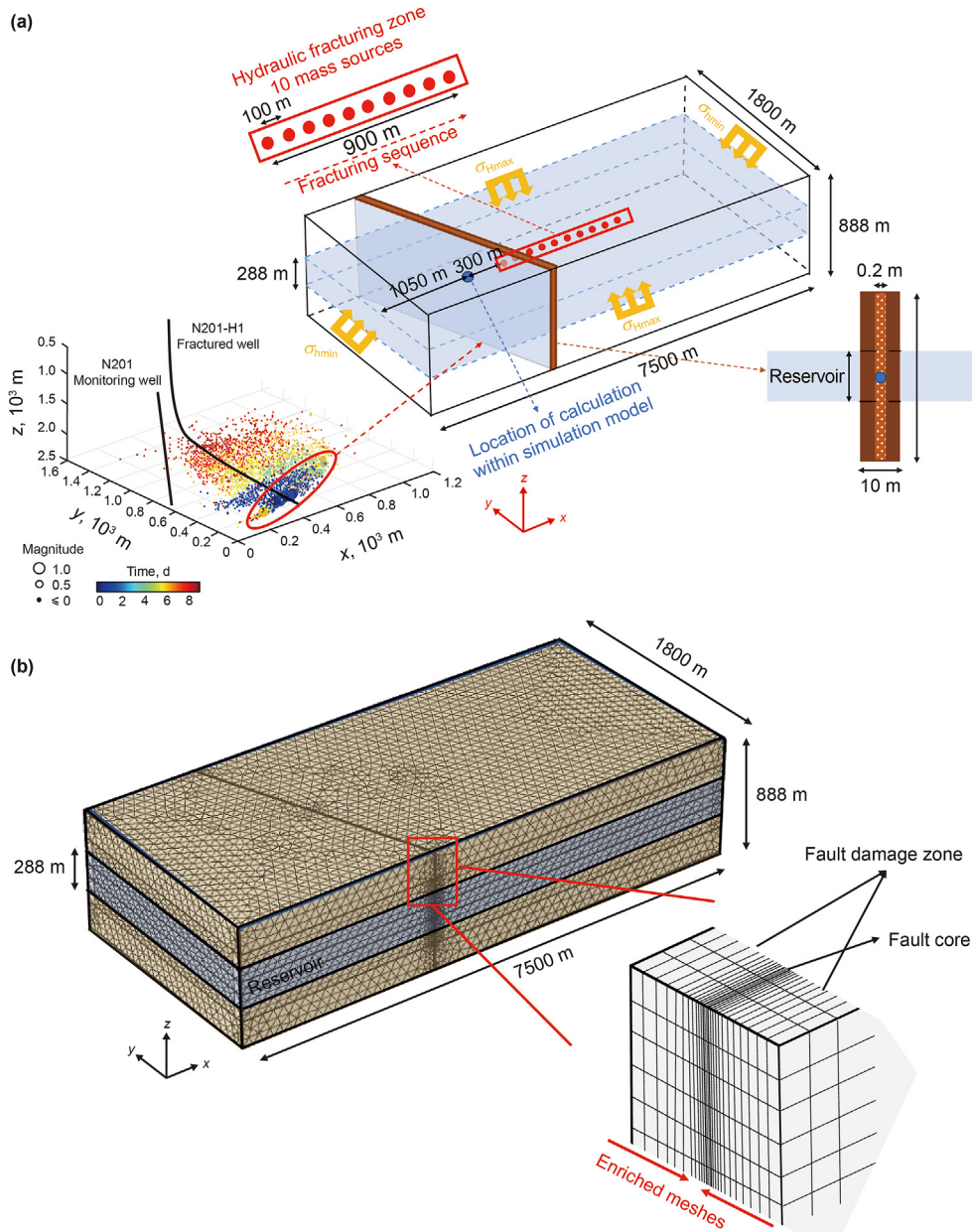**Fig. 3.** Position of the horizontal well Ning 201-H1 and its well plan.

Fig. 4. Three-dimensional schematic (**a**) and meshing schematic (**b**) of the numerical model.

period to represent the effects of fluid transfer in the fault and reservoir (Zhang et al., 2020). To achieve a strike-slip faulting regime, the gradients of the three principal stresses, σ_v, σ_{Hmax}, and σ_{hmin}, were set to 21.0, 28.0, and 18.0 kPa/m, respectively, and the pore pressure gradient was set to 12.5 kPa/m. The stresses along the z, y and x directions in the 3D simulation model (σ_v, σ_{Hmax}, and σ_{hmin}) therefore reached 49.0, 56.0 and 36.0 MPa, respectively.

Representative parameters were selected from the literature and are listed in Table 1.

4. Model results

A slip-oriented fault in the nearly critical state must exist for an injection-induced seismic event to occur. The CFS criterion only addresses fault stability without differentiating whether the resulting fault slip is seismic (stick-sliding) or aseismic (creep-

sliding) depending on the value of the critical fault stiffness k_{crit} (Goodfellow et al., 2015; Guglielmi et al., 2015; Spagnuolo et al., 2016; Fan et al., 2019; Yehya et al., 2022). Thus, in this section, we first confirmed the fault in the slip state by calculating the changes in Coulomb stresses (Eq. (17)) and then evaluated whether fault slip could trigger earthquakes by estimating the modified fault critical stiffness (Eq. (17)). Here, we analysed the evolution of the CFS and k_{crit} values of the faults during and after HF operation and specifically focused on the significant impact of the change rate of effective stress on the likelihood of induced earthquakes. The specific location of analysis is the low-permeability fault core at the junction position in the fault and the reservoir. The following subsections explain the obtained simulation results.

Table 1
Model parameter.

| Parameter	Value	Reference
Young's modulus E, GPa	20	Cui et al. (2018); Zhang et al. (2008)
Poisson's ratio υ	0.25	
Porosity ϕ_m	0.1	
Reservoir permeability k_r, m^2	1.0×10^{-15}	Chen et al. (2019); Yehya et al. (2018)
Fault zone permeability k_f, m^2	1.0×10^{-14}	
Fault core permeability k_c, m^2	1.0×10^{-18}	
z-direction stress σ_v, kPa/m	21.0	Fan et al. (2019); Zhang et al. (2020)
x-direction stress σ_{hmin}, kPa/m	18.0	
y-direction stress σ_{Hmax}, kPa/m	28.0	
Rate of hydraulic fracturing Q, m^3/s	9.0	
Initial pore pressure P_0, kPa/m	12.5	
Velocity-weakening parameters $a-b$	-0.3×10^{-2}	Marone (1998)
Normalized frictional parameter α	1.0×10^{-2}	
Characteristic slip distance d_c, m	0.01	
Initial slip velocity v_0, m/s	1.0×10^{-6}	Aharonov and Scholz (2018); Ito and Ikari (2016)
Compressibility of the fluid χ_f, Pa^{-1}	4.0×10^{-10}	
Compressibility of the matrix χ_p, Pa^{-1}	1.0×10^{-4}	

4.1. Evolution of the fault normal stress and pore pressure

Throughout the whole process of HF operation, the effective stress variation of the fault core can be separated into four stages due to the net impact of the changes in the normal stress and pore pressure on the effective stress, as shown in Fig. 5.

(i) At the first stage, because the position of the first fracturing well is far from the fault, no variation of fluid pressure in the fault core observed (as shown in Fig. 5) as the fluid diffuses into the reservoir but pore pressure front has not yet arrived at the fault. However, the increase in the pore pressure of the fault core associated with fluid injection causes volumetric expansion in the perturbed part of the reservoir, which exerts an added compression effect on the low-permeability fault due to the stress transfer effects of the poroelastic rock matrix (Segall and Fitzgerald, 1998; Fan et al., 2019; Villa and Singh, 2020). As shown in Fig. 5, the normal stress of the fault increases at an increasing rate during each injection period and increases relatively slowly during each shut-in period. The evolution of the effective stress of the fault core is dominated by that of the normal stress as the change

in the pore pressure remains zero. The effective stress of the fault core thus increases at an increasing rate during each injection period and increases relatively slowly during the shut-off period.

(ii) At the second stage, the fluid diffuses and arrives at the fault, and the pore pressure of the fault core starts to increase at a certain rate. The decrease in the distance between the fracturing well and fault leads to a more pronounced poroelastic effect in the reservoir. The compression effects on the fault become more significant, resulting in a higher increasing rate of the normal stress; thus, the normal stress of the fault core increases more significantly than that at the first stage. The increasing rate of the normal stress is far higher than that of pore pressure at this stage. Thus, the effective stress of the fault core increases at a more significant increasing rate during each injection period and shut-off period relative to the first stage.

(iii) At the third stage, the normal stress of the fault core still increases but at a lower increasing rate due to the stress release effects when the whole HF operation is stopped. The pore pressure of the fault core continues to increase with fluid diffusion. However, the change rate of the normal stress
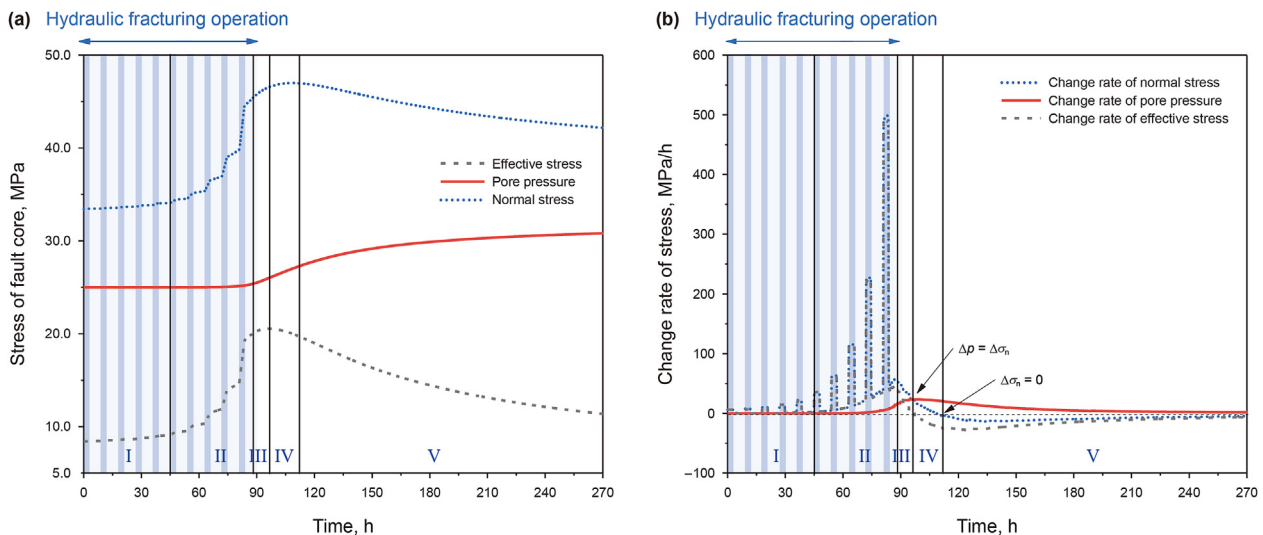
Fig. 5. Evolution of the effective stress and its components (i.e., the pore pressure and normal stress) in the fault core. (**a**) Change in stress; (**b**) Change rate of stress.

of the fault core is still much higher than that of the pore pressure. As a result, a lower enhancing rate is observed for the effective stress of the fault core at this stage.

(iv) At the fourth stage, both the normal stress and pore pressure of the fault core increase at a lower increasing rate due to further stress release effects and fluid diffusion. At this stage, the change rate of the pore pressure of the fault core is higher than that of the normal stress. Thus, the change rate of effective stress changes to negative and the effective stress of the fault core rapidly decreases.

(v) At the fifth stage, the normal stress of the fault core further decreases with increasing stress release due to the self-equilibrium effects in the entire geological system. The pore pressure of the fault core increases at a lower increasing rate. The effective stress of the fault core decreases at an increasing rate but still keeps negative and the change rate of effective stress gradually approaches 0.

4.2. Coulomb stress changes

For a critically stressed fault, any positive change in the CFS value affects the fault response to the perturbation and could lead to fault slip. The fault exhibits a tendency to slide and possesses the prerequisite for triggering seismic slip (stick-sliding) once the shear stress is larger than its shear friction strength, i.e., the CFS value remains positive. In the simulation model, the friction coefficient was set to 0.5, and the shear friction strength varied with effective stress based on the Mohr−Coulomb model. As shown in Fig. 6, the shear stress in fault core sharply decreased with increasing friction strength during the injection period of HF operation and gradually increased with decreasing friction strength during the period after HF operation.

Thus, during each injection period of HF operation, the CFS value of the fault core sharply decreased with a sudden drop in the rate (ΔCFS), indicating that the slipping fault generated a stability response to injection with decreasing shear stress and increasing friction strength. However, before nearly 70 days, the CFS value remained positive, indicating fault slip. After nearly 70 days, the CFS value became negative with a negative change in CFS. After nearly 90 days, the CFS value increased with a positive change in CFS and became positive again after nearly 195 days. During and after the

whole process of HF operation, CFS alternated between positive and negative values, which indicates that the fault was sliding or occurred in a critical sliding state. Thus, it is necessary to evaluate whether the slip state of the fault facilitates the triggering of seismicity.

4.3. Evolution of the critical stiffness

4.3.1. Impact of the effective stress magnitude (classical critical stiffness changes)

The classical critical stiffness, proportional to the change in the effective stress, can be separated into five stages as shown in Fig. 7.

(i) At the first stage, the effective stress of the fault core increases during each injection period and increases relatively slowly during each shut-off period. According to the classical critical stiffness criterion (Rice, 1993), the evolution of the critical stiffness is proportional to the change in the effective
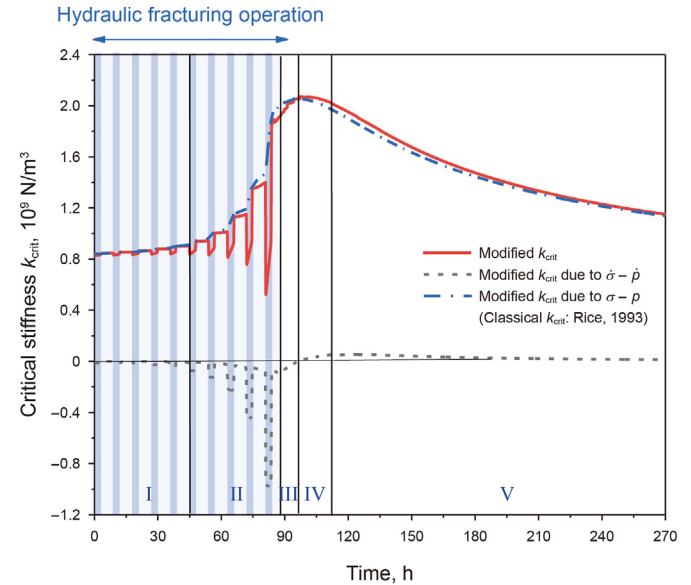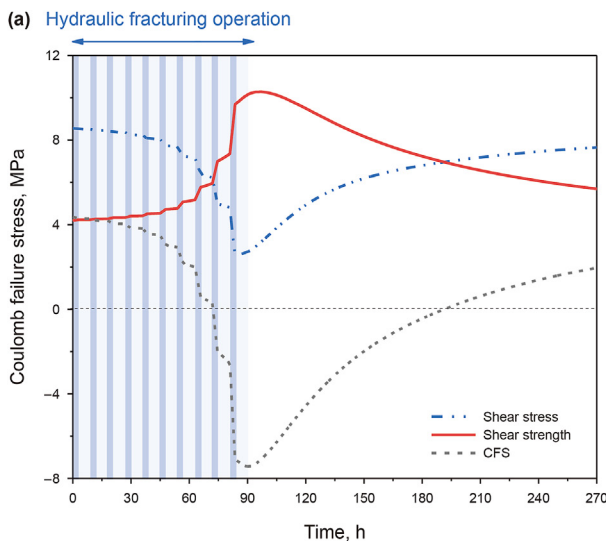

Fig. 7. The evolution of the modified critical stiffness, and its components, i.e. magnitude and change rate of effective stress.
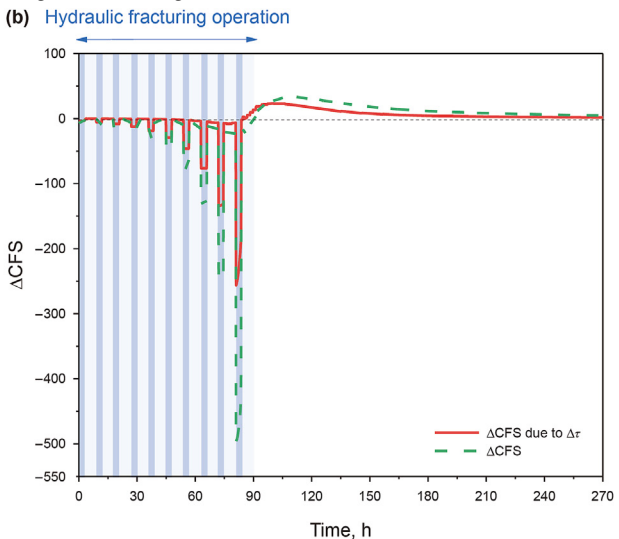

Fig. 6. Evolution of the CFS value and the solution term, i.e., shear stress and shear friction strength. (**a**) Change in CFS; (**b**) Change rate of CFS.

stress. The classical critical stiffness of the fault core thus increases during each injection period and increases relatively slowly during each shut-off period with increasing magnitude of the effective stress of the fault core, which triggers fault slip and rises the likelihood of induced seismicity.

(ii) At the second stage, as fluid front approaches to the fault core, the effective stress increases dramaticly than that of previous stage with increasing compression effects. Also a significant enhancement in classical critical stiffness is also observedduring injection and shut-off periods, indicating that the fault causes more significant seismic slip in response to fracturing and increases the risk of triggering seismicity.

(iii) At the third stage, the effective stress of the fault core continues to increase, but it increases at a slow decreasing rate after the end of HF operation, increasing the classical critical stiffness. At this stage, the classical critical stiffness rises to the maximum value, i.e., to the highest risk of inducing earthquakes.

(iv) At the fourth stage, the effective stress of the fault core shows a dramatic delining due to the rapidly decreases causing by the increased gas pressure. As a result, a negative value in the changing rate of effective stress appears. Correspondingly, the classical critical stiffness of the fault core decreases driving aseismic slip of the fault and reducing the likelihood of induced seismicity.

(v) At the fifth stage, the effective stress of the fault core decreases at an increasing rate but still keeps negative. The classical critical stiffness of the fault core decreases with decreasing effective stress of the fault core, which facilitates aseismic slip of the fault and decreases the risk of triggering seismicity.
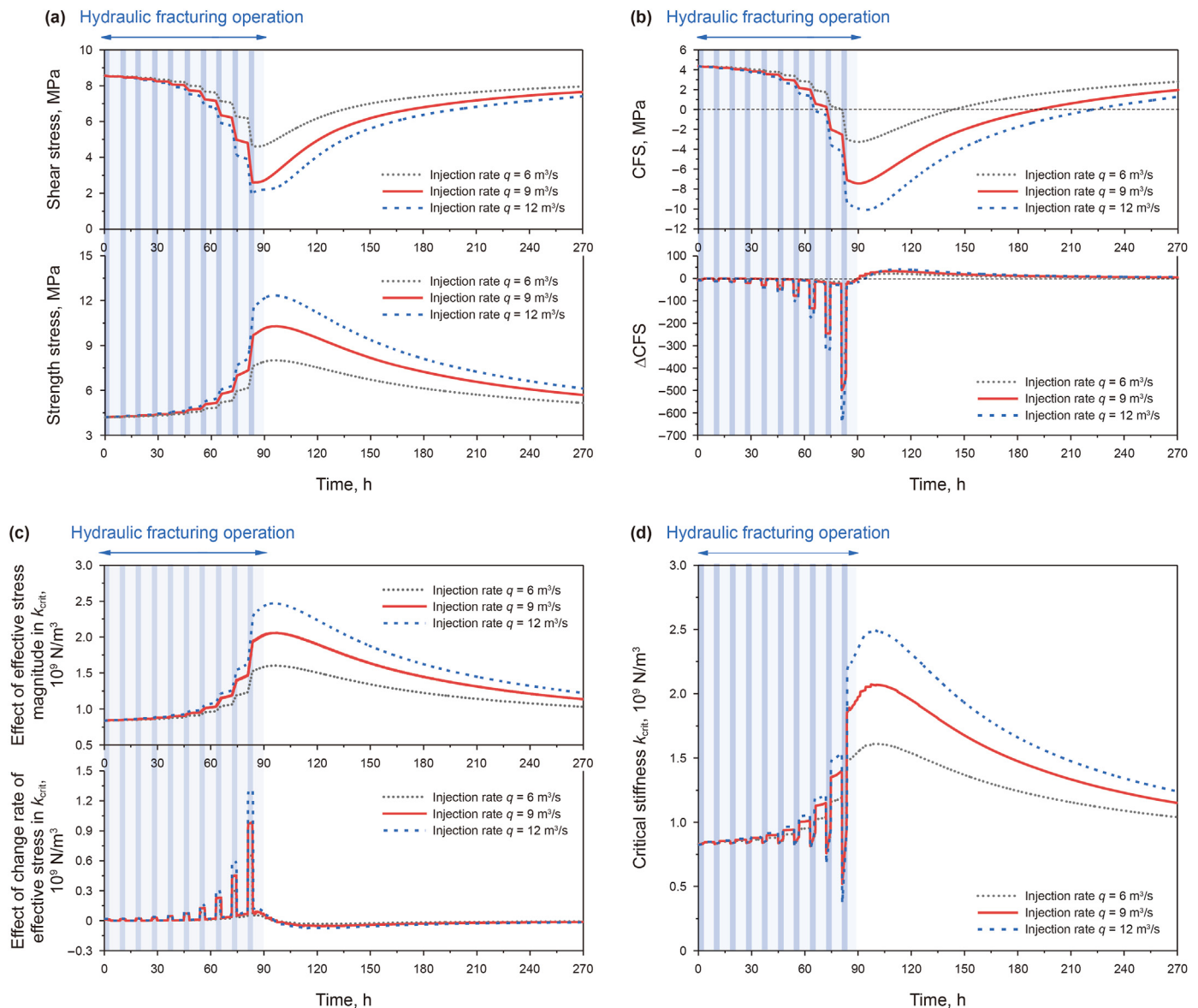
Fig. 8. Comparison of stability profiles for the different injection rates. (**a**) Shear stress and shear friction strength; (**b**) Magnitude and change rate of CFS; (**c**) Effect of the effective stress magnitude in critical stiffness and effect of the change rate of effective stress in critical stiffness; (**d**) Evolution of the critical stiffness.

4.3.2. Impact of the change rate of effective stress

The dominate role of change rate of effective stress on the critical stiffness of the fault can also be divided into five stages as shown in Fig. 7.

(i) At the first stage, the change rate of effective stress of the fault core suddenly increases at the start of each injection period and suddenly decreases at the end of each injection period. The critical stiffness of the fault core is negatively correlated with change rate of effective stress based on Eq. (17). During each fracturing injection period, the change rate of effective stress suddenly increases at the beginning of injection, reducing the critical stiffness and driving aseismic slip of the fault. The change rate of effective stress abruptly decreases at the end of injection, increasing the critical stiffness and facilitating seismic slip of the fault.

(ii) At the second stage, the change rate of effective stress of the fault core increases more significantly than that at the first stage at the beginning of each fracturing period, lowering the critical stiffness and driving aseismic slip of the fault. The change rate of effective stress decreases more significantly at the end of each fracturing period, increasing the critical stiffness and promoting seismic slip of the fault.

(iii) At the third stage, the change rate of effective stress decreases rapidly, increasing the critical stiffness of the fault core and triggering seismic slip.

(iv) At the fourth stage, the change rate of effective stress of the fault core becomes negative and decrease slower than that at the third stage, enhancing the critical stiffness of the fault core and initiating slip of the fault. At this stage, the critical stiffness increases to its maximum value, which is the state with the highest risk of triggering seismicity.

(v) At the fifth stage, the change rate of effective stress gradually increases and approaches 0 (but remained negative), reducing the critical stiffness of the fault core and driving aseismic slip of the fault.

4.3.3. Modified critical stiffness changes

As illustrated above, the modified fault critical stiffness (Eq. (17)) are impacted by both magnitude and change rate of effective stress.

The former term enhances the value of fault critical stiffness, and the later term decreases the value in our case study. The modified variation in the critical stiffness of the fault core can be separated into five stages, as shown in Fig. 7:

(i) At the first stage, the critical stiffness decreases at the beginning of each injection period, triggering aseismic slip of the fault and reducing the likelihood of seismicity, as controlled by the increasing rate of the effective stress. At each constant-injection stage, the critical stiffness slightly increases, dominated by the increased effective stress magnitude. The critical stiffness suddenly increases at the end of each injection period, mainly due to the decreasing rate of the effective stress, resulting in fault seismic slip and enhancing the potential of seismicity.

(ii) At the second stage, no significant difference of critical stiffness of the fault core is observed when compared with the first stage. This is mainly because that variation in pore pressure of fault core is much lower than that in the normal stress. Meanwhile, the extrusion effect applied on the fault core enhances dramaticly than at the first stage as the pore pressure is approaching. The critical stiffness thus increases and then decreases more intensely at this stage relative to the first stage, resulting in more dramatic seismic slip and aseismic slip of the fault, respectively.

(iii) At the third stage, the increase in effective stress magnitude and the decrease in change rate of effective stress jointly increase the critical stiffness, which promotes seismic slip of the fault.

(iv) At the fourth stage, the critical stiffness is reduced by the decreasing effective stress while raised by the decreasing change rate. As a result, the critical stiffness first increases and then decreases due to the competition effect of the magnitude of, and change rate in effective stress. At this stage, the modified critical stiffness increases to its maximum value, which is the highest risk of triggering earthquakes.

(v) At the fifth stage, the decrease in effective stress magnitude and the increase in the change rate of effective stress jointly reduce the critical stiffness, thus driving aseismic slip of the fault and reducing the likelihood of earthquakes.
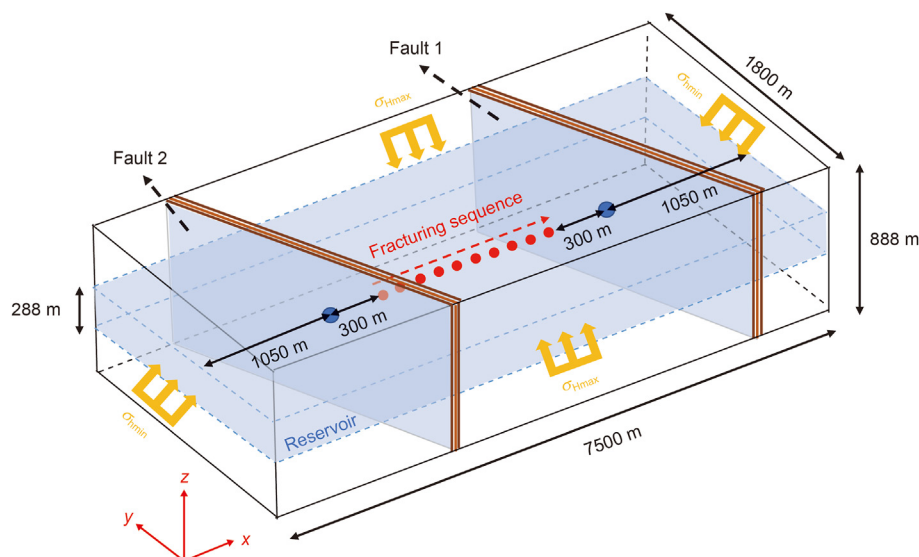

Fig. 9. Schematic of a numerical model with two fault positions.

5. Discussion

In this section, we analyse the impact of the hydrogeological factors, i.e., fault permeability distribution, fault position, and HF region, and HF injection rate on the evolution of seismicity during hydraulic fracturing.

5.1. Injection rate in hydraulic fracturing

To investigate the impact of HF operation on the likelihood of seismic slip of the fault (i.e., evolution of the critical stiffness), three injection rates were designed under a constant-injection scenario: 6, 9, and 12 m^3/s.

As illustrated in Fig. 8(a), the increased shear strength and the decreased shear stress during each injection period of HF operation jointly reduced CFS and drove it towards a negative value, triggering a stability response of fault slip to fracturing. The shear strength increased, and the shear stress decreased after the end of

HF operation, enhancing CFS and converting it to a positive value. Additionally, the stability response of the fault core with a higher injection rate occurred earlier during HF operation, manifested as more significant changes in the stress strength and shear stress. Reactivation of the fault core (CFS>0) occurred later after the end of HF operation. As shown in Fig. 8(a) and (b), all three cases of different injection rates provided prerequisites for fault slip at the beginning of HF operation, i.e., CFS>0.

It can be observed that a higher injection rate would lead to a significant value of the critical stiffness of the fault core when injection was suddenly started and stopped during HF operation, as shown in Fig. 8(c) and (d), respectively. The critical stiffness of the fault core with a higher injection rate decreased faster because of its larger enhancement in the change rate of effective stress of the fault core when injection was suddenly started, triggering a stability response of the fault core to injection. On the contrary, when injection was suddenly stopped, the critical stiffness of the fault core at a higher injection rate increased faster with a larger decrement in
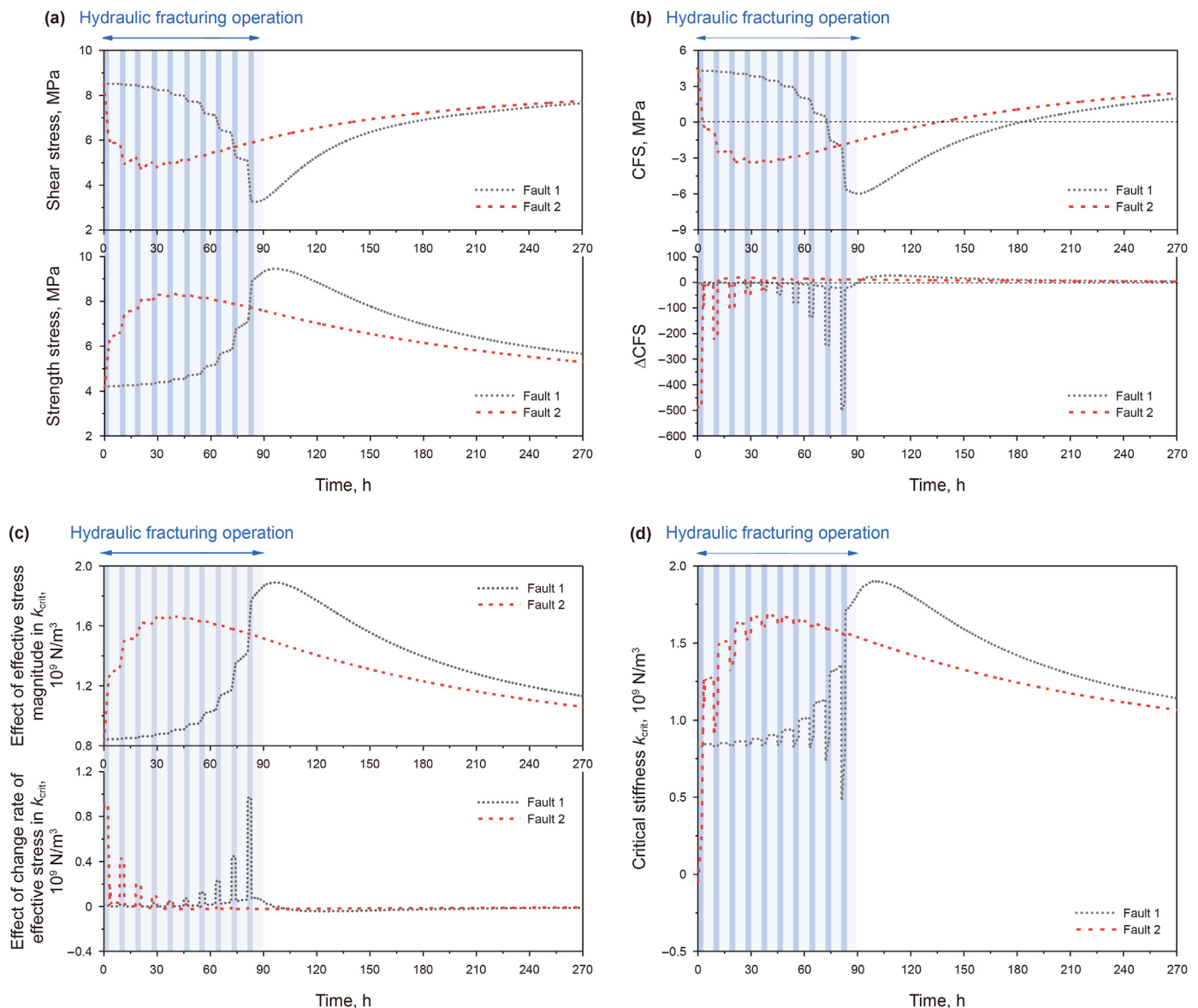
Fig. 10. Analysis of the stress for Fault 1 and Fault 2. (**a**) Shear stress and shear friction strength; (**b**) Magnitude and change rate of CFS; (**c**) Effect of effective stress magnitude in critical stiffness and effect of change rate of effective stress in critical stiffness; (**d**) Evolution of the critical stiffness.
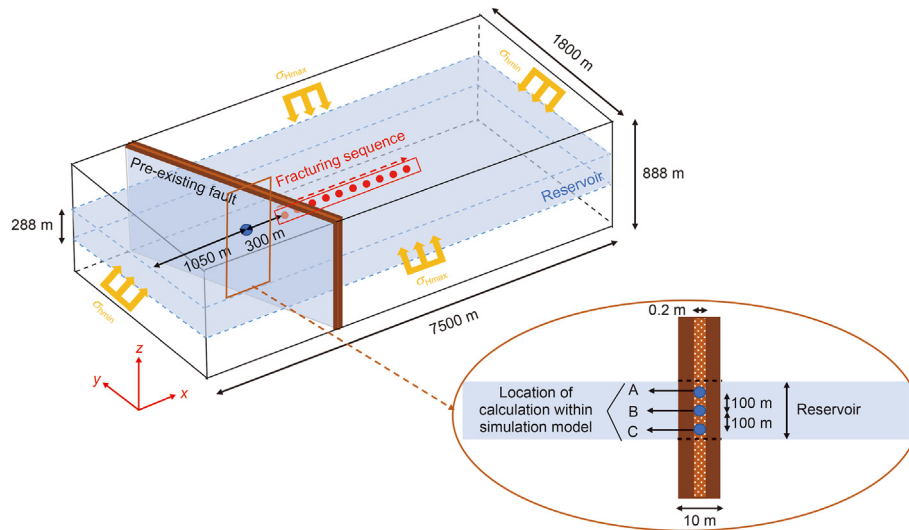
Fig. 11. Schematic of a numerical model with different locations along the fault in detail.

the change rate of effective stress of the fault core. After the end of the entire HF process, the critical stiffness of the fault core with a higher injection rate increased more significantly due to the larger increase in the effective stress and reached its maximum, exerting the most unstable impact of the fault and thus more likely to excite fault seismic slip.

We could conclude that a higher injection rate could stabilize the slipping fault earlier and more significantly during HF operation. However, a higher injection rate during HF operation could cause greater enhancements in CFS and critical stiffness of the fault core after the end of HF operation, resulting in reactivation of the fault relatively late and potentially yielding a higher likelihood of seismic slip of the fault. To avoid seismicity of the fault under HF operation, the injection rate should be reduced. However, during the period of HF operation, to avoid seismicity of the fault relatively far away from the fracturing well, the injection rate should be high enough to create a normal compressive stress that can stabilize the fault. Thus, an optimum injection strategy based on different factors needs more extensive study. In future studies, the injection rate should be estimated, and the permeability distribution and the relative positions of faults and injection wells should be considered.

5.2. Fault position and hydraulic fracturing region

We next consider two cases in which ten injection wells are activated one after the other gradually towards Fault 1 or far away from Fault 2 (Fig. 9) to investigate the response at various relative locations of the fault and fracturing wells to HF operation.

As shown in Fig. 10(a), the shear stress of Fault 2 decreased earlier than that of Fault 1 as the nearer fracturing wells at the early time of HF operation. The shear strength of Fault 2 increased earlier than that of Fault 1 due to the nearer fracturing wells at the early time of HF operation. The CFS of Fault 2 converted to a negative value earlier than that of Fault 1, representing that Fault 2 turns to stability state earlier, due to the earlier stability response of Fault 2 to injection relative to Fault 1 and the shorter distance between the fracturing wells and Fault 2. Two locations of the fault exhibited reactivation behaviour, as shown in Fig. 10(a) and (b), which occurred earlier in Fault 1 than in Fault 2.

As shown in Fig. 10(c) and (d), the critical stiffness of Fault 2 increased, triggering an unstable response of the fault at the early time of HF operation, due to the decreased change rate of effective

stress of the fault core during each stopping period of injection. During HF operation, the critical stiffness of Fault 2 always exceeded Fault 1. After HF operation, the critical stiffness of Fault 1 increased more notably with decreasing change rate of effective stress of the fault core at the end of the last injection. Therefore, after HF operation, the critical stiffness of Fault 1 exceeded Fault 2. This is an interesting observation regarding the role of the fault location and how the likelihood of induced earthquake evolution with injection time differs depending on the relative position of the fracturing wells and fault. The case of Fault 2 was characterized by earlier dramatic variation in the critical stiffness, due to a more intense increased effective stress at early time of HF operation and reached its maximum value (highest risk of triggering earthquakes) at the HF operation stage. However, the critical stiffness of Fault 1 rapidly increased after HF operation and reached the maximum value and triggered a higher probability of unstable fault slip.

5.3. Different positions along the fault

In this section, three positions were selected to illustrate the impact of different positions in the fault core on critical stiffness evolution, as shown in Fig. 11. Among them, position B refers to the junction of the fault and the reservoir, while positions A and C located 100 m above and below position B, respectively (Fig. 11).

The CFS value at all three positions decreased with decreasing shear stress and increasing normal stress, thereby inducing a stability response of the slipping fault to injection during HF operation. The shear stress and normal stress of the fault core at position B changed more significantly after HF operation, respectively, which resulted in the largest decrease in CFS. The CFS value at position B thus changed and reactivated the fault later than that at positions A and C, as illustrated in Fig. 12(a) and (b), respectively. When comparing the cases of positions A and C, the value at position C changed more notably than that at position A during and after HF operation, respectively, indicating a greater response in the lower region of the fault to HF operation.

In addition, the evolution of the critical stiffness at position C in the fault core was more notable than that at position A, as the initial value of the critical stiffness was increased, as shown in Fig. 12(c) and (d), respectively. The critical stiffness of the fault core at position B increased more significantly than that at positions A and C due to the most intense reduction in the change rate of effective
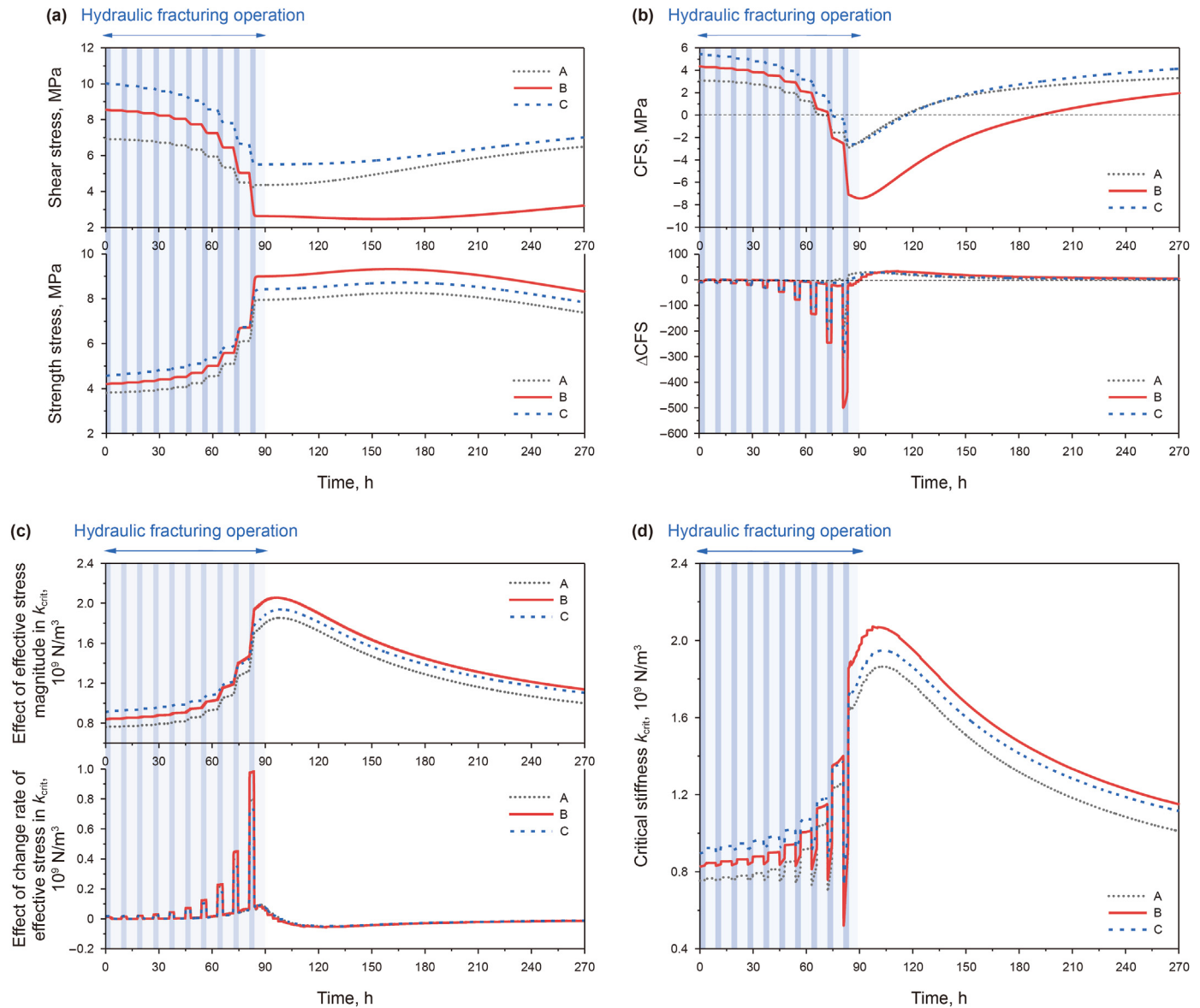
Fig. 12. Comparison of the stability profiles for the different locations along the fault. (**a**) Shear stress and shear friction strength; (**b**) Magnitude and change rate of CFS; (**c**) Effect of effective stress magnitude in critical stiffness and effect of change rate of effective stress in critical stiffness; (**d**) Evolution of the critical stiffness.

stress after HF operation, which is more potentially to cause unstable sliding induced by faults. The upper region (position A) of the fault core, as mentioned above, could stabilize the slipping fault earlier and more significantly during HF operation.

The lower region (position C) of the fault core could reactivate the fault more obviously after the end of HF operation. However, the region at the junction between the reservoir and fault (position C) could yield a greater enhancement in the critical stiffness of the fault core after the end of HF operation, which is the region most likely to induce seismicity.

5.4. Explanation of the field observations and model verification

Field microseismic data, as shown in Fig. 13, were obtained by eight downhole geophones in the pre-existing vertical well Ning 201 (Zhang et al., 2020). Fig. 13(a) shows the evolution of the number of microseismic events, cumulation moment and injected fluid volume with fracturing time across 10 fracturing stages.

Fig. 13(b) shows the number of microseismic events during the pumping of each stage and the following shut-in period. Although the injected volume at each fracturing stage remained the same, an extremely large increment in seismic moments occurred after stage 2, resulting in severe casing deformation. Zhang et al. (2020) analysed the monitored microseismic events and divided them into two groups based on the locations relative to the pre-existing fault (fault-related events and fracture-related events).

As indicated by the numerous fault-related events (red-filled circles) in Fig. 13, many fault-related microseismic events occurred at the first four stages. The number of fault-related events gradually decreased as the fracturing operation moved away from the fault and decreased sharply after stage 3 (Zhang et al., 2020) as shown in Fig. 13(b). As discussed in chapter 5.2, the correlation between the fault position and HF sequence could be explained by the variation in the critical stiffness gradually decreasing as the fracturing process moved away from the fault (Fig. 13(b)). The fault near the fracturing operation region exhibited a higher potential of
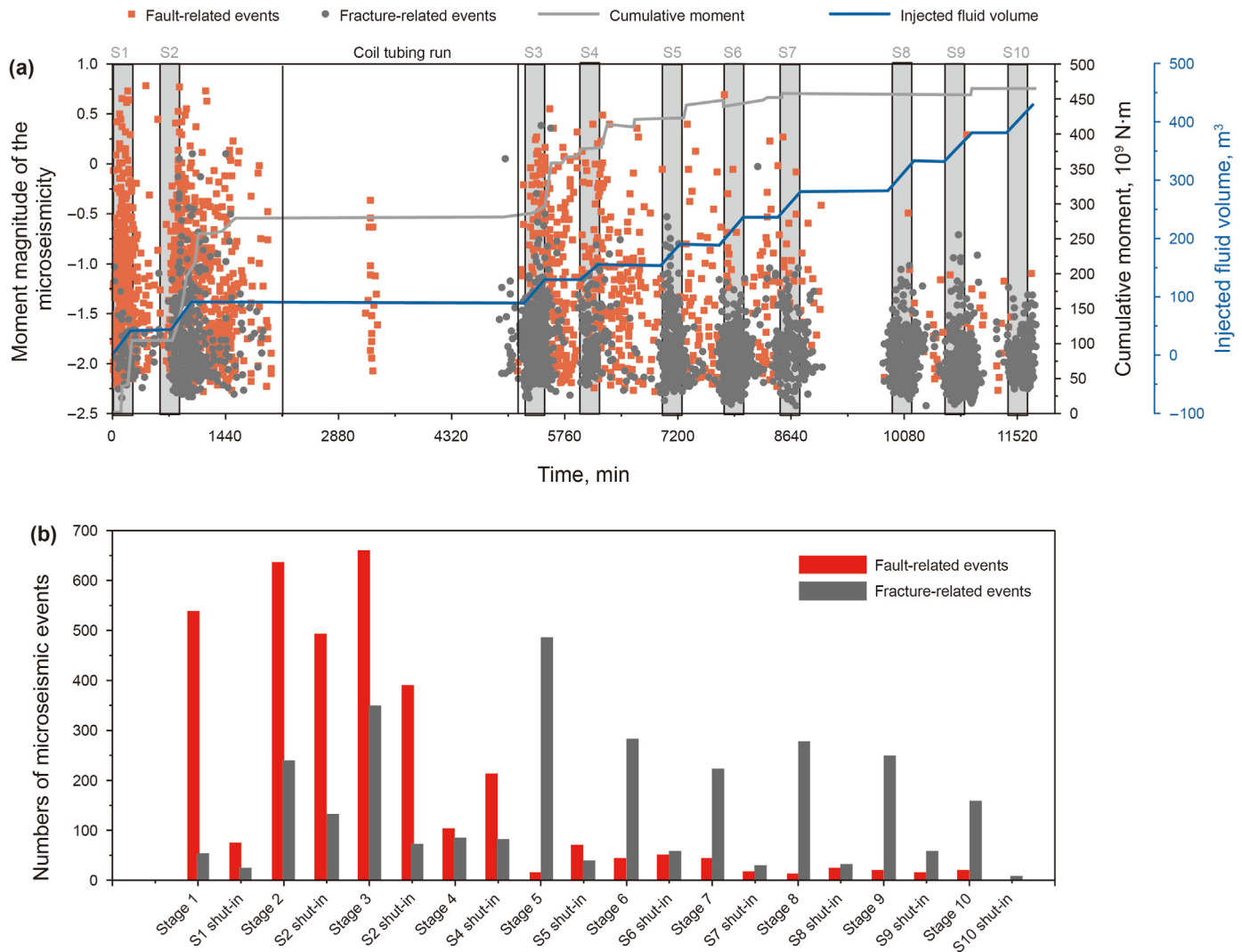
Fig. 13. Field microseismic events monitored via pre-existing vertical well Ning 201 (Zhang et al., 2020). (**a**) The number of microseismic events, cumulation moment, and injected fluid volume with fracturing time. The red-filled circles and black-filled circles represent fault-related events and fracturing-related events, respectively. The grey and blue lines denote cumulation moments and fluid injection volume, respectively. (**b**) The number of microseismic events during the pumping stages and the following shut-in stages.

triggering earthquakes.

Additionally, as shown in the blue and grey lines of Fig. 13(a), the cumulative moment was positively correlated with the volume of injected fluid, and the largest increment in seismic moments always occurred at the end of injection at each fracturing stage (a sudden decrease in the fluid injection rate). This fascinating relationship between the variation in the fluid injection rate and the sudden increase in seismic moments could be explained by the proposed critical stiffness criterion. The critical stiffness first decreased, stabilizing the fault at the beginning of fluid injection at each fracturing stage. The critical stiffness then gradually increased at the fracturing stage under a constant fluid injection rate. The critical stiffness greatly increased and reached its maximum value at the fracturing stage after the fluid injection rate suddenly decreased at the end of each fracturing stage. Thus, the occurrence of a large seismic moment at the end of the fracturing stage in the field could explain why the critical stiffness increases as the injection rate suddenly reduces.

6. Conclusions

A three dimensional fully coupled poroelastic model consisting of a reservoir and pre-existing faults was established to estimate the likelihood of induced earthquakes during multistage HF operations based on the engineering background of the Longmaxi Formation in the Sichuan Basin, China. CFS was first used to determine whether the fault exhibited a slip trend as a prerequisite for triggering seismic slip during HF operation. The modified critical stiffness model was proposed for estimating the likelihood of induced earthquakes during and after HF operation. The critical stiffness was positive correlated to the effective stress of fault and was negative correlated to the change rate of effective stress. Additionally, the fault response to stress perturbation resulting from HF operation was affected by the injection rate during fracturing, fault orientation, and position along the fault with respect to HF operations. Based on this work, the following conclusions could be drawn:

(a) At each fracturing stage, the critical stiffness decreased at the beginning of each injection period, slightly increased at each

constant-injection stage, and then suddenly increased with the injection rate suddenly stopped. Then, the critical stiffness varied more dramatically as the fracturing stages approached the fault. After HF operation was stopped, the critical stiffness increased to its maximum value, reaching the highest likelihood of triggering earthquakes. Finally, the critical stiffness decreased, driving aseismic slip of the fault and reducing the likelihood of earthquakes.

(b) The change rate of effective stress dominated the critical stiffness evolution when the injection rate suddenly varied at each fracturing stage. Conversely, the effective stress magnitude played a major role in the variation in the critical stiffness at the constant-injection stage during each fracturing period. The critical stiffness reached its minimum value after the first period of injection. Conversely, the critical stiffness arrived at its maximum value after the stopping of each fracturing stage. After the end of HF operation, the critical stiffness of the fault core triggered the maximum likelihood of yielding a seismic response.

(c) Locating the fracturing stage far away from the fault and reducing the rate of injection during HF operation are the best options for minimizing seismicity. The junction area between the reservoir and fault is likely to a more unstable position of the fault during HF operation, while the fault core above the reservoir is safer than that below the reservoir.

(d) The largest moment magnitude after HF operation was stopped and the phenomenon that the fault near the fracturing operation region exhibited a higher potential of triggering earthquakes in the shale gas exploration field in Longmaxi Formation, Sichuan Basin, China, could be suitably explained by modified critical stiffness.

CRediT authorship contribution statement

Zi-Han Sun: Conceptualization, Data curation, Formal analysis, Investigation, Methodology, Validation, Visualization, Writing − original draft, Writing − review & editing, Software. **Ming-Guang Che:** Conceptualization, Data curation, Formal analysis, Project administration, Supervision, Validation, Visualization. **Li-Hong Zhu:** Conceptualization, Data curation, Formal analysis, Project administration, Supervision, Validation, Visualization. **Shu-Juan Zhang:** Conceptualization, Data curation, Formal analysis, Supervision, Validation, Visualization. **Ji-Yuan Lu:** Conceptualization, Data curation, Formal analysis, Project administration, Supervision, Validation, Visualization. **Chang-Yu Jin:** Conceptualization, Data curation, Formal analysis, Investigation, Methodology, Supervision, Validation, Visualization, Writing − review & editing.

Declaration of competing interest

The authors declare that they have no known competing financial interests or personal relationships that could have appeared to influence the work reported in this paper.

Acknowledgments

References

Aharonov, E., Scholz, C.H., 2018. A physics-based rock friction constitutive law: steady state friction. J. Geophys. Res. Solid Earth 123 (2), 1591−1614. https://doi.org/10.1002/2016JB013829.

Alghannam, M., Juanes, R., 2020. Understanding rate effects in injection-induced earthquakes. Nat. Commun. 11 (1), 1−6. https://doi.org/10.1038/s41467-020-16860-y.

Anderson, E.M., 1905. The dynamics of faulting. Trans. Edinb. Geol. Soc. 8 (3), 387−402. https://doi.org/10.1144/transed.8.3.387.

Atkinson, G.M., Eaton, D.W., Igonin, N., 2020. Developments in understanding seismicity triggered by hydraulic fracturing. Nat. Rev. Earth Environ. 1, 264−277. https://doi.org/10.1038/s43017-020-0049-7.

Bachmann, C.E., Wiemer, S., Woessner, J., et al., 2011. Statistical analysis of the induced basel 2006 earthquake sequence: introducing a probability-based monitoring approach for enhanced geothermal systems. Geophys. J. Int. 186 (2), 793−807. https://doi.org/10.1111/j.1365-246X.2011.05068.x.

Bao, X.W., Eaton, D.W., 2016. Fault activation by hydraulic fracturing in western Canada. Science 354 (6318), 1406−1409. https://doi.org/10.1126/science.aag2583.

Barbour, A.J., Norbeck, J.H., Rubinstein, J.L., 2017. The effects of varying injection rates in Osage County, Oklahoma, on the 2016 Mw 5.8 Pawnee Earthquake. Seismol Res. Lett. 88 (4), 1040−1053. https://doi.org/10.1785/0220170003.

Benson, P., Austria, D.C., Gehne, S., et al., 2020. Laboratory simulations of fluid-induced seismicity, hydraulic fracture, and fluid flow. Geomech Energy Environ. 24, 100169. https://doi.org/10.1016/j.gete.2019.100169.

Biot, M.A., 1941. General theory of three-dimensional consolidation. J. Appl. Phys. 12, 155−164.

Brudy, M., Zoback, M.D., Fuchs, K., et al., 1997. Estimation of the complete stress tensor to 8 km depth in the KTB scientific drill holes: implications for crustal strength. J. Geophys. Res. Solid Earth 102 (B8), 18453−18475. https://doi.org/10.1029/96jb02942.

Brudzinski, M.R., Kozowska, M., 2019. Seismicity induced by hydraulic fracturing and wastewater disposal in the Appalachian Basin, USA: a review. Acta Geophys. 67 (1), 351−364. https://doi.org/10.1007/s11600-019-00249-7.

Caine, J.S., Evans, J.P., Forster, C.B., 1996. Fault zone architecture and permeability structure. Geology 24 (11), 1025−1028. https://doi.org/10.1130/0091-7613(1996)024<1025:FZAAPS>2.3.CO;2.

Celleri, H.M., Sánchez, M., 2021. Hydraulic fracture propagation barriers induced by weak interfaces in anisotropic rocks. Int. J. Numer. Anal. Methods GeoMech. 45 (14), 2155−2173. https://doi.org/10.1002/nag.3260.

Chang, K.W., Segall, P., 2016a. Injection-induced seismicity on basement faults including poroelastic stressing. J. Geophys. Res. Solid Earth 121 (4), 2708−2726. https://doi.org/10.1002/2015jb012561.

Chang, K.W., Segall, P., 2016b. Seismicity on basement faults induced by simultaneous fluid injection-extraction. Pure Appl. Geophys. 173 (8), 2621−2636. https://doi.org/10.1007/s00024-016-1319-7.

Chen, D., Li, N., Wang, E., 2021. Reliability assessment of the hydraulic fracturing process in coal mine based on the analysis of micro-seismic source parameters. Nat. Resour. Res. 30 (3), 2317−2332. https://doi.org/10.1007/s11053-021-09840-6.

Chen, J., Niemeijer, A.R., 2017. Seismogenic potential of a gouge-filled fault and the criterion for its slip stability: constraints from a microphysical model. J. Geophys. Res. Solid Earth 122 (12), 9658−9688. https://doi.org/10.1002/2017JB014226.

Chen, T., Feng, X.T., Cui, G., Tan, Y.L., et al., 2019. Experimental study of permeability change of organic-rich gas shales under high effective stress. J. Nat. Gas Sci. Eng. 64, 1−14. https://doi.org/10.1016/j.jngse.2019.01.014.

Cueto-Felgueroso, L., Santillán, D., Mosquera, J.C., 2017. Stick-slip dynamics of flow-induced seismicity on rate and state faults. Geophys. Res. Lett. 44 (9), 4098−4106. https://doi.org/10.1002/2016gl072045.

Cui, G., Liu, J., Wei, M., et al., 2018. Why shale permeability changes under variable effective stresses: new insights. Fuel 213, 55−71. https://doi.org/10.1016/j.fuel.2017.10.068.

Darcy, H., 1856. Les fontaines publiques de la ville de Dijon Rep. Dalmont, Paris.

Davies, R., Foulger, G., Bindley, A., et al., 2013. Induced seismicity and hydraulic fracturing for the recovery of hydrocarbons. Mar. Petrol. Geol. 45 (4), 171−185. https://doi.org/10.1016/j.marpetgeo.2013.03.016.

Davis, C., Fisk, J.M., 2017. Mitigating risks from fracking-related earthquakes: assessing state regulatory decisions. Soc. Nat. Resour. 30 (8), 1009−1025. https://doi.org/10.1080/08941920.2016.1273415.

Deng, K., Liu, Y., Harrington, R.M., 2016. Poroelastic stress triggering of the December 2013 Crooked Lake, Alberta, induced seismicity sequence. Geophys. Res. Lett. 43 (16), 8482−8491. https://doi.org/10.1002/2016GL070421.

Detournay, E., Cheng, H.D., 1993. Fundamentals of poroelasticity. Anal Des Methods 140 (1), 113−171.

Dieterich, J.H., 1972. Time-dependent friction in rocks. J. Geophys. Res. 77 (20), 3690−3697. https://doi.org/10.1029/JB077i020p03690.

Dieterich, James. H., 1978. Time-dependent friction and the mechanics of stick-slip. Pure Appl Geophys. 116, 790−806. https://doi.org/10.1007/BF00876539.

Ellsworth, W.L., 2013. Injection-induced earthquakes. Science 341 (6142), 1225942. https://doi.org/10.1126/science.1225942.

Evans, K.F., Zappone, A., Kraft, T., et al., 2012. A survey of the induced seismic responses to fluid injection in geothermal and CO₂ reservoirs in Europe.

Geothermics 41, 30–54. https://doi.org/10.1016/j.geothermics.2011.08.002.

Eyre, T.S., Eaton, D.W., Garagash, D.I., et al., 2019. The role of aseismic slip in hydraulic fracturing-induced seismicity. Sci. Adv. 5 (8), eaav7172. https://doi.org/10.1126/sciadv.aav7172.

Fan, Z.Q., Eichhubl, P., Newell, P., 2019. Basement fault reactivation by fluid injection into sedimentary reservoirs: poroelastic effects. J. Geophys. Res. Solid Earth 124 (7), 7354–7369. https://doi.org/10.1029/2018jb017062.

Fisher, M., Warpinski, N., 2012. Hydraulic-fracture-height growth: real data. SPE Prod. Oper. 27 (1), 8–19. https://doi.org/10.2118/145949-MS.

Frohlich, C., 2012. Two-year survey comparing earthquake activity and injection-well locations in the Barnett Shale, Texas. Proc. Natl. Acad. Sci. USA 109 (35), 13934–13938. https://doi.org/10.1073/pnas.1207728109.

Galloway, E., Hauck, T., Corlett, H., et al., 2018. Faults and associated karst collapse suggest conduits for fluid flow that influence hydraulic fracturing-induced seismicity. Proc. Natl. Acad. Sci. U.S.A. 115 (43), e10003–e10012. https://doi.org/10.1073/pnas.1807549115.

Gan, Q., Lei, Q., 2020. Induced fault reactivation by thermal perturbation in enhanced geothermal systems. Geothermics 86 (101814), 1–12. https://doi.org/10.1016/j.geothermics.2020.101814.

Goodfellow, S.D., Nasseri, M.H.B., Maxwell, S.C., 2015. Hydraulic fracture energy budget: insights from the laboratory. Geophys. Res. Lett. 42 (9), 3179–3187. https://doi.org/10.1002/2015GL063093.

Gu, J.C., Rice, J.R., Ruina, A.L., 1984. Slip motion and stability of a single degree of freedom elastic system with rate and state dependent friction. J. Mech. Phys. Solid. 32 (3), 167–196. https://doi.org/10.1016/0022-5096(84)90007-3.

Gudmundsson, A., 2022. The propagation paths of fluid-driven fractures in layered and faulted rocks. Geol. Mag. 159 (11–12), 1978–2001. https://doi.org/10.1017/S0016756822000826.

Guglielmi, Y., Cappa, F., Avouac, J.P., et al., 2015. Seismicity triggered by fluid injection–induced aseismic slip. Science 348 (6240), 1224–1226. https://doi.org/10.1126/science.aab0476.

Guo, L., Jiang, Z.X., Zhang, J.C., et al., 2011. Paleoenvironment of Lower Silurian black shale and its significance to the potential of shale gas, southeast of Chongqing, China. Energy Explor. Exploit. 29 (5), 597–616. https://doi.org/10.1260/0144-5987.29.5.597.

Hiquake, 2023. https://inducedearthquakes.org/.

Holland, A.A., 2013. Earthquakes triggered by hydraulic fracturing in south-central Oklahoma. Bull. Seismol. Soc. Am. 103 (3), 1784–1792. https://doi.org/10.1785/0120120109.

Hui, G., Chen, S., Chen, Z., et al., 2021. Influence of hydrological communication between basement-rooted faults and hydraulic fractures on induced seismicity: a case study. J. Petrol. Sci. Eng. 206, 109040. https://doi.org/10.1016/j.petrol.2021.109040.

Hutka, G.A., Cacace, M., Hofmann, H., et al., 2023. Numerical investigation of the effect of fluid pressurization rate on laboratory-scale injection-induced fault slip. Sci. Rep. 13, 4437. https://doi.org/10.1038/s41598-023-30866-8.

Improta, L., Valoroso, L., Piccinini, D., et al., 2015. A detailed analysis of wastewater-induced seismicity in the Val d'Agri oil field (Italy). Geophys. Res. Lett. 42, 2682–2690. https://doi.org/10.1002/2015GL063369.

Ito, Y., Ikari, M.J., 2016. Velocity- and slip-dependent weakening in simulated fault gouge: implications for multimode fault slip. Geophys. Res. Lett. 42 (21), 9247–9254. https://doi.org/10.1002/2015GL065829.

Iverson, R.M., 2005. Regulation of landslide motion by dilatancy and pore pressure feedback. J. Geophys. Res. Earth Surf. 110 (F2), F02015. https://doi.org/10.1029/2004jf000268.

Ji, Y.L., Wang, L., Hofmann, H., et al., 2022. High-rate fluid injection reduces the nucleation length of laboratory earthquakes on critically stressed faults in granite. Geophys. Res. Lett. 49 (23). https://doi.org/10.1029/2022GL100418.

Jia, Y., Song, C., Liu, R., 2022. The frictional restrengthening and permeability evolution of slipping shale fractures during seismic cycles. Rock Mech. Rock Eng. 55 (4), 1791–1805. https://doi.org/10.1007/s00603-021-02751-1.

Jiang, S., Tang, X., Long, S., et al., 2017. Reservoir quality, gas accumulation and completion quality assessment of Silurian Longmaxi marine shale gas play in the Sichuan Basin, China. J. Nat. Gas Sci. Eng. 39, 203–215. https://doi.org/10.1016/j.jngse.2016.08.079.

Keranen, K.M., Weingarten, M., Abers, G.A., et al., 2014. Induced earthquakes. Sharp increase in central Oklahoma seismicity since 2008 induced by massive wastewater injection. Science 345 (6195), 448–451. https://doi.org/10.1126/science.1255802.

Kim, K.H., Ree, J.H., Kim, Y., et al., 2018. Assessing whether the 2017 Mw 5.4 Pohang earthquake in South Korea was an induced event. Science 360 (6392), 1007–1009. https://doi.org/10.1126/science.aat6081.

Kim, W.Y., 2013. Induced seismicity associated with fluid injection into a deep well in Youngstown, Ohio. J. Geophys. Res. Solid Earth 118 (7), 3506–3518. https://doi.org/10.1002/jgrb.50247.

Leeman, J.R., Saffer, D.M., Scuderi, M.M., 2016. Laboratory observations of slow earthquakes and the spectrum of tectonic fault slip modes. Nat. Commun. 7, 11104. https://doi.org/10.1038/ncomms11104.

Lei, X., Huang, D., Su, J., et al., 2017. Fault reactivation and earthquakes with magnitudes of up to Mw4.7 induced by shale-gas hydraulic fracturing in Sichuan Basin, China. Sci. Rep. 7 (1), 7971. https://doi.org/10.1038/s41598-017-08557-y.

Li, Q., Konstantinovskaya, E., Zhmodik, A., et al., 2023. Interaction of natural and hydraulic fractures: the impact on reservoir pressure buildup and risk of shear fault reactivation in the Upper Devonian Duvernay Formation, Fox Creek, Alberta. Geomech. Geophys. Geo. Energy Ge. Resour. 9 (1), 21. https://doi.org/10.1007/s40948-023-00537-z.

Liang, C., Jiang, Z.X., Zhang, C.M., et al., 2014. The shale characteristics and shale gas exploration prospects of the Lower Silurian Longmaxi shale, Sichuan Basin, South China. J. Nat. Gas Sci. Eng. 21, 636–648. https://doi.org/10.1016/j.jngse.2014.09.034.

Linker, M.F., Dieterich, J.H., 1992. Effects of variable normal stress on rock friction: observations and constitutive equations. J. Geophys. Res. 97 (B4), 4923–4940. https://doi.org/10.1016/0148-9062(93)90292-L.

Lu, G., Hao, S.W., Elsworth, D., 2023. Precursory predictors of the onset of stick-slip frictional instability. Int. J. Solid Struct. 264, 112119. https://doi.org/10.1016/j.ijsolstr.2023.112119.

Marone, C., 1998. Laboratory-derived friction laws and their application to seismic faulting. Annu. Rev. Earth Planet Sci. 26, 643–696. https://doi.org/10.1146/annurev.earth.26.1.643.

Meng, M., Ge, H., Shen, Y., et al., 2021. Evaluation of the pore structure variation during hydraulic fracturing in marine shale reservoirs. ASME. J. Energy Resour. Technol. 143 (8), 083002. https://doi.org/10.1115/1.4048872.

Mignan, A., Landtwing, D., Kstli, P., et al., 2015. Induced seismicity risk analysis of the 2006 Basel, Switzerland, Enhanced Geothermal System project: influence of uncertainties on risk mitigation. Geothermics 53, 133–146. https://doi.org/10.1016/j.geothermics.2014.05.007.

Min, K.B., Rutqvist, J., Elsworth, D., 2009. Chemically and mechanically mediated influences on the transport and mechanical characteristics of rock fractures. Int. J. Rock Mech. Min. Sci. 46 (1), 80–89. https://doi.org/10.1016/j.ijrmms.2008.04.002.

Mitsui, Y., Cocco, M., 2010. The role of porosity evolution and fluid flow in frictional instabilities: a parametric study using a spring-slider dynamic system. Geophys. Res. Lett. 37 (23). https://doi.org/10.1029/2010gl045672.

Pampillon, P., Santillan, D., Mosquera, J.C., 2018. Dynamic and quasi-dynamic modeling of injection-induced earthquakes in poroelastic media. J. Geophys. Res. Solid Earth 123 (7), 5730–5759. https://doi.org/10.1029/2018jb015533.

Peduzzi, P., Harding, R., 2013. Gas fracking: can we safely squeeze the rocks? Environ. Dev. 6, 86–99. https://doi.org/10.1016/j.envdev.2012.12.001.

Rezlerova, E., Brennan, J.K., Lisal, M., 2021. Methane and carbon dioxide indual-porosityorganic matter: molecular simulations of adsorption and diffusion. AIChE J. 67 (3), e16655. https://doi.org/10.1002/aic.16655.

Rice, J.R., Cleary, M.P., 1976. Some basic stress diffusion solutions for fluid-saturated elastic porous media with compressible constituents. Rev. Geophys. 14 (2), 227–241. https://doi.org/10.1029/RG014i002p00227.

Rice, J.R., 1993. Spatio-temporal complexity of slip on a fault. J. Geophys. Res. Atmos. 98 (B6), 9885–9907. https://doi.org/10.1029/93jb00191.

Rice, J.R., 2006. Heating and weakening of faults during earthquake slip. J. Geophys. Res. 111 (B5), B05311. https://doi.org/10.1029/2005jb004006.

Rice, J.R., Ruina, A.L., 1983. Stability of steady frictional slipping. J. Appl. Mech. 50 (2), 343–349. https://doi.org/10.1115/1.3167042.

Ruina, A., 1983. Slip instability and state variable friction laws. J. Geophys. Res. 88 (B12), 10359–10370. https://doi.org/10.1029/JB088iB12p10359.

Schultz, R., Stern, V., Gu, Y.J., 2014. An investigation of seismicity clustered near the Cordel Field, west central Alberta, and its relation to a nearby disposal well. J. Geophys. Res. Solid Earth 119 (4), 3410–3423. https://doi.org/10.1002/2013jb010836.

Schultz, R., Wang, R.J., Gu, Y.J., 2017. A seismological overview of the induced earthquakes in the Duvernay play near Fox Creek, Alberta. J. Geophys. Res. Solid Earth 122 (1), 492–505. https://doi.org/10.1002/2016jb013570.

Segall, P., Fitzgerald, S.D., 1998. A note on induced stress changes in hydrocarbon and geothermal reservoirs. Tectonophysics 289 (1), 117–128. https://doi.org/10.1016/S0040-1951(97)00311-9.

Segall, P., Lu, S., 2015. Injection-induced seismicity: poroelastic and earthquake nucleation effects. J. Geophys. Res. Solid Earth 120 (7), 5082–5103. https://doi.org/10.1002/2015jb012060.

Segall, P., Rice, J.R., 1995. Dilatancy, compaction, and slip instability of a fluid-infiltrated fault. J. Geophys. Res. 1002 (B11), 22155–22172. https://doi.org/10.1029/95JB02403.

Shan, K., Zhang, Y., Zheng, Y., et al., 2021. Effect of fault distribution on hydraulic fracturing: insights from the laboratory. Renew. Energy 163, 1817–1830. https://doi.org/10.1016/j.renene.2020.10.083.

Sheng, M., Chu, R., Peng, Z., et al., 2022. Earthquakes triggered by fluid diffusion and boosted by fault reactivation in weiyuan, China due to hydraulic fracturing. J. Geophys. Res. Solid Earth (5), 127. https://doi.org/10.1029/2021JB022963.

Sheng, M.H., Chu, R.S., Ni, S.D., et al., 2020. Source parameters of three moderate size earthquakes in weiyuan, China, and their relations to shale gas hydraulic fracturing. J. Geophys. Res. Solid Earth 125 (10). https://doi.org/10.1029/2020jb019932.

Spagnuolo, E., Nielsen, S., Violay, M., et al., 2016. An empirically based steady state friction law and implications for fault stability. Geophys. Res. Lett. 43 (7), 3263–3271. https://doi.org/10.1002/2016GL067881.

Sun, X., Yang, P., Zhang, Z., 2017. A study of earthquakes induced by water injection in the Changning salt mine area, SW China. J. Asian Earth Sci. 136, 102–109. https://doi.org/10.1016/j.jseaes.2017.01.030.

Sun, Z., Elsworth, D., Cui. G., 2023. Impacts of rates of change in effective stress and of inertial effects on fault slip behavior: new insights into injection-induced earthquakes. J. Geophys. Res. Solid Earth. under review.

Tang, L., Lu, Z., Zhang, M., et al., 2018. Seismicity induced by simultaneous abrupt changes of injection rate and well pressure in Hutubi gas field. J. Geophys. Res. Solid Earth 123 (7), 5929–5944. https://doi.org/10.1029/2018jb015863.

Teodor, M.A., Ardéshir, G., 2000. Theory of Elasticity for Scientists and Engineers. Springer. ISBN 0-8176-4072-X.

Terzaghi, K.v., 1923. Die berechnung der durchlassigkeitsziffer des tones aus dem verlauf der hydrodynamischen spannungserscheinungen. Sitzungsberichte der Akademie der Wissenschaften in Wien, Mathematisch-Naturwissenschaftliche Klasse. Abteilung IIa 132 (3–4), 125–138.

Townend, J., Zoback, M.D., 2000. How faulting keeps the crust strong. Geology 28 (5), 399–402. https://doi.org/10.1130/0091-7613(2000)28<399: Hfktcs>2.0.Co;2.

Tullis, T.E., Weeks, J.D., 1986. Constitutive behavior and stability of frictional sliding of granite. Pure Appl. Geophys. 124 (3), 383–414. https://doi.org/10.1007/BF00877209.

van den Ende, M.P.A., Chen, J., Ampuero, J.P., et al., 2018. A comparison between rate-and-state friction and microphysical models, based on numerical simulations of fault slip. Tectonophysics 733, 273–295. https://doi.org/10.1016/j.tecto.2017.11.040.

van Thienen-Visser, K., Roholl, J.A., van Kempen, B.M.M., et al., 2018. Categorizing seismic risk for the onshore gas fields in The Netherlands. Eng. Geol. 237, 198–207. https://doi.org/10.1016/j.enggeo.2018.02.004.

Vilarrasa, V., Roman, M., Sohrab, G., 2016. Geomechanical analysis of the influence of CO$_2$ injection location on fault stability. J. Rock Mech. Geotech. Eng. 8, 805–818. https://doi.org/10.1016/j.jrmge.2016.06.006.

Villa, V., Singh, R.P., 2020. Hydraulic fracturing operation for oil and gas production and associated earthquake activities across the USA. Environ. Earth Sci. 79 (11), 271. https://doi.org/10.1007/s12665-020-09008-0.

Vrolijk, P.J., Urai, J.L., Kettermann, M., 2016. Clay smear: review of mechanisms and applications. J. Struct. Geol. 86, 95–152. https://doi.org/10.1016/j.jsg.2015.09.006.

Wang, M., Yang, H., Fang, L., et al., 2020. Shallow faults reactivated by hydraulic fracturing: the 2019 Weiyuan earthquake sequences in Sichuan, China. Seismol Res. Lett. 91 (6). https://doi.org/10.1785/0220200174.

Wang, Y., Li, X., Zhang, Y.X., et al., 2016. Gas shale hydraulic fracturing: a numerical investigation of the fracturing network evolution in the Silurian Longmaxi formation in the southeast of Sichuan Basin, China, using a coupled FSD

approach. Environ. Earth Sci. 75 (14), 1093. https://doi.org/10.1007/s12665-016-5696-0.

Warpinski, N.R.R., Du, J., Zimmer, U., 2012. Measurements of hydraulic-fracture-induced seismicity in gas shales. SPE Prod. Oper. 27 (3), 240–252. https://doi.org/10.2118/151597-PA.

Xu, J.C., Guo, C.H., Wei, M.Z., et al., 2015. Production performance analysis for composite shale gas reservoir considering multiple transport mechanisms. J. Nat. Gas Sci. Eng. 26, 382–395. https://doi.org/10.1016/j.jngse.2015.05.033.

Yehya, A., Basbous, J., Maalouf, E., 2022. Analysis of the hydrogeological conditions affecting fault response to nearby hydraulic fracturing. J. Geophys. Res. Solid Earth 127 (10). https://doi.org/10.1029/2022jb024881.

Yehya, A., Yang, Z., Rice, J.R., 2018. Effect of fault architecture and permeability evolution on response to fluid injection. J. Geophys. Res. Solid Earth. https://doi.org/10.1029/2018JB016550.

Zhang, F.S., Yin, Z.R., Chen, Z.W., et al., 2020. Fault reactivation and induced seismicity during multistage hydraulic fracturing: microseismic analysis and geomechanical modeling. SPE J. 25 (2), 692–711. https://doi.org/10.2118/199883-PA.

Zhang, H.B., Liu, J.S., Elsworth, D., 2008. How sorption-induced matrix deformation affects gas flow in coal seams: a new FE model. Int. J. Rock Mech. Min. Sci. 45 (8), 1226–1236. https://doi.org/10.1016/j.ijrmms.2007.11.007.

Zhao, L., Qin, X., Han, D.H., et al., 2016. Rock-physics modeling for the elastic properties of organic shale at different maturity stages. Geophysics 81 (5), D527–D541. https://doi.org/10.1190/geo2015-0713.1.

Zhao, L., Qin, X., Zhang, J., et al., 2018. An effective reservoir parameter for seismic characterization of organic shale reservoir. Surv. Geophys. 39 (3), 509–541. https://doi.org/10.1007/s10712-017-9456-9.

Zoback, M.D., Harjes, H.P., 1997. Injection-induced earthquakes and crustal stress at 9 km depth at the KTB deep drilling site, Germany. J. Geophys. Res. Solid Earth 102 (B8), 18477–18491. https://doi.org/10.1029/96jb02814.

Zou, C., Dong, D., Wang, S., et al., 2010. Geological characteristics and resource potential of shale gas in China. Petrol. Explor. Dev. 37 (6), 641–653. https://doi.org/10.1016/S1876-3804(11)60001-3.